The viral fitness and intrinsic pathogenicity of dominant SARS-CoV-2 Omicron sublineages BA.1, BA.2, and BA.5

Huiping Shuai,[a,i] Jasper Fuk-Woo Chan,[a,b,c,d,e,f,i] Bingjie Hu,[a,i] Yue Chai,[a,i] Chaemin Yoon,[a,i] Huan Liu,[a] Yuanchen Liu,[a] Jialu Shi,[a] Tianrenzheng Zhu,[a] Jing-Chu Hu,[g] Ye-fan Hu,[g] Yuxin Hou,[a] Xiner Huang,[a] Terrence Tsz-Tai Yuen,[a] Yang Wang,[a] Jinjin Zhang,[a] Yao Xia,[a] Lin-Lei Chen,[a] Jian-Piao Cai,[a] Anna Jinxia Zhang,[a,c] Shuofeng Yuan,[a,b,c] Jie Zhou,[a,c] Bao-Zhong Zhang,[h] Jian-Dong Huang,[g] Kwok-Yung Yuen,[a,b,c,d,e,f] Kelvin Kai-Wang To,[a,b,c,e,f] and Hin Chu[a,b,c,j,*]

[a]State Key Laboratory of Emerging Infectious Diseases, Department of Microbiology, and Carol Yu Centre for Infection, School of Clinical Medicine, Li Ka Shing Faculty of Medicine, The University of Hong Kong, Pokfulam, Hong Kong Special Administrative Region, China
[b]Department of Infectious Disease and Microbiology, The University of Hong Kong-Shenzhen Hospital, Shenzhen, Guangdong Province, China
[c]Centre for Virology, Vaccinology and Therapeutics, Hong Kong Science and Technology Park, Hong Kong Special Administrative Region, China
[d]Academician Workstation of Hainan Province, Hainan Medical University-The University of Hong Kong Joint Laboratory of Tropical Infectious Diseases, Hainan Medical University, Haikou, Hainan, China; and The University of Hong Kong, Pokfulam, Hong Kong Special Administrative Region, China
[e]Department of Microbiology, Queen Mary Hospital, Pokfulam, Hong Kong Special Administrative Region, China
[f]Guangzhou Laboratory, Guangdong Province, China
[g]School of Biomedical Sciences, Li Ka Shing Faculty of Medicine, The University of Hong Kong, Pokfulam, Hong Kong Special Administrative Region, China
[h]CAS Key Laboratory of Quantitative Engineering Biology, Shenzhen Institute of Synthetic Biology, Shenzhen Institutes of Advanced Technology, Chinese Academy of Sciences, Shenzhen, Guangdong Province, China

eBioMedicine
2023;95: 104753
Published Online xxx
https://doi.org/10.1016/j.ebiom.2023.104753

Summary

Background Among the Omicron sublineages that have emerged, BA.1, BA.2, BA.5, and their related sublineages have resulted in the largest number of infections. While recent studies demonstrated that all Omicron sublineages robustly escape neutralizing antibody response, it remains unclear on whether these Omicron sublineages share any pattern of evolutionary trajectory on their replication efficiency and intrinsic pathogenicity along the respiratory tract.

Methods We compared the virological features, replication capacity of dominant Omicron sublineages BA.1, BA.2 and BA.5 in the human nasal epithelium, and characterized their pathogenicity in K18-hACE2, A129, young C57BL/6, and aged C57BL/6 mice.

Findings We found that BA.5 replicated most robustly, followed by BA.2 and BA.1, in the differentiated human nasal epithelium. Consistently, BA.5 infection resulted in higher viral gene copies, infectious viral titres and more abundant viral antigen expression in the nasal turbinates of the infected K18-hACE2 transgenic mice. In contrast, the Omicron sublineages are continuously attenuated in lungs of infected K18-hACE2 and C57BL/6 mice, leading to decreased pathogenicity. Nevertheless, lung manifestations remain severe in Omicron sublineages-infected A129 and aged C57BL/6 mice.

Interpretation Our results suggested that the Omicron sublineages might be gaining intrinsic replication fitness in the upper respiratory tract, therefore highlighting the importance of global surveillance of the emergence of hyper-transmissive Omicron sublineages. On the contrary, replication and intrinsic pathogenicity of Omicron is suggested to be further attenuated in the lower respiratory tract. Effective vaccination and other precautions should be in place to prevent severe infections in the immunocompromised populations at risk.

Funding A full list of funding bodies that contributed to this study can be found in the Acknowledgements section.

*Corresponding author. State Key Laboratory of Emerging Infectious Diseases, Department of Microbiology, and Carol Yu Centre for Infection, School of Clinical Medicine, Li Ka Shing Faculty of Medicine, The University of Hong Kong, Pokfulam, Hong Kong Special Administrative Region, China.
E-mail address: hinchu@hku.hk (H. Chu).
[i]These authors contributed equally to this work.
[j]Lead contact.

Keywords: SARS-CoV-2; COVID-19; Omicron; BA.5; Replication; Pathogenicity; Spike; Evolution trajectory; Animal models; Mice

Research in context

Evidence before this study

We searched PubMed on 18th April, 2023, with no starting date limitations, using the terms "SARS-CoV-2" and "Omicron sublineages" and "mice" for articles in English. From the 19 articles available, it did not reveal any report that investigated the evolution trajectory of the replication fitness and pathogenicity of Omicron sublineages BA.1, BA.2, BA.2.12.1, BA.4 and BA.5 in vivo. We also searched "Omicron BA.5" and "replication fitness" and it yielded six studies showing BA.5 replication in human airway epithelium, hACE2 transgenic mice, and hamsters, but not other animal models.

Added value of this study

Our study reveals the divergent replication capacity of the sequentially emerged Omicron sublineages (BA.1, BA.2, BA.2.12.1, BA.4 and BA.5) in the upper and lower respiratory tract. We show that the sequentially-emerged Omicron sublineages might be gaining intrinsic replication fitness and replicate more robustly than ancestral SARS-CoV-2 in the differentiated human nasal epithelial cells. In the infected animals, while the Omicron sublineages are replicating more efficiently in the upper respiratory tract, their pathogenicity in the lung continues to attenuate. Using the aged mice and type-I interferon signaling deficient mice, we show that lung damage caused by Omicron BA.5 remains severe in the immunocompromised animal models.

Implications of all the available evidence

The emergence of Omicron sublineages led to the surge of multiple waves of widespread SARS-CoV-2 infections globally. Our findings suggest that the Omicron sublineages have been gaining intrinsic replication fitness in the upper airway, highlighting the importance of global surveillance on emerging SARS-CoV-2 subvariants, especially on the early detection of hyper-transmissive subvariants. Although replication and intrinsic pathogenicity of the Omicron sublineages continue to attenuate in the lower respiratory tract, the risk of severe infection remains high in the immunocompromised populations. Given the current relaxation of COVID-19-related social restrictions, development of effective nasal vaccines and implementation of preventive measures should be in place to protect the elderlies and immunocompromised patients.

Introduction

Reported after Alpha (PANGO lineage B.1.1.7), Beta (B.1.351), Gamma (P.1), and Delta (B.1.617.2), Omicron (B.1.1.529) was designated as the fifth SARS-CoV-2 variant of concern (VOC) by the World Health Organization on November 26th, 2021 and has quickly replaced Delta as the predominant circulating SARS-CoV-2 variant. Omicron BA.1 (B.1.1.529.1) contains a large number of mutations when compared with ancestral SARS-CoV-2, including 30 substitutions, three short deletions, and one insertion in the spike protein. Due to these changes, BA.1 demonstrated substantially altered virological features including reduced spike cleavage, attenuated pathogenicity, and robust immune evasion to neutralization antibodies.[1–9] Continuous surveillance of Omicron evolution revealed that BA.1 was replaced by BA.2 and related sublineages, which became the predominant circulating SARS-CoV-2 strains until mid-2022, and were subsequently replaced by BA.5 and related sublineages.

Recent clinical investigations revealed a decreased pathogenicity of BA.1 and BA.2 when compared to previous VOCs,[10–14] which are in agreement with previous in vitro and in vivo studies reported from us and others.[4,8,15,16] However, clinical severity of BA.5 and its related sublineages remain incompletely understood. Moreover, Omicron and its sublineages have remained as the most prevalent SARS-CoV-2 variant until today. Whether these sequentially emerged Omicron sublineages share a pattern of evolutionary trajectory on their intrinsic infectability and pathogenicity remains unclear. In this study, we systemically compared the virological features, replication capacity in the upper and lower respiratory tract, and intrinsic pathogenicity of BA.1, BA.2, BA.4, and BA.5 sublineages. We demonstrated that the virus replication of Omicron sublineages is becoming increasingly robust in primary human nasal epithelial cells and in the nasal turbinates of K18-hACE2, young C57BL/6, aged C57BL/6, and A129 mouse models. Meanwhile, the virus replication of Omicron sublineages has a trend of further attenuation in the lungs of K18-hACE2 and young C57BL/6 mice, leading to attenuated pathogenicity. Notably, Omicron sublineages can still cause severe diseases in the lungs of A129 and aged C57BL/6 mice, suggesting preventative measures should be in place for the highly susceptible populations including the elderlies and immunocompromised patients.

Methods

Experimental model and subject details

Viruses and biosafety

Wild type SARS-CoV-2 HKU-001a (GenBank: MT230904), B.1.351/Beta (GISAID: EPI_ISL_2423556), B.1.617.2/Delta (GenBank: OM212471), BA.1 (GenBank: OM212472), BA.2 (GISAID: EPI_ISL_9845731), BA.2.12.1 (GISAID: EPI_ISL_13777659), BA.4.1 (GISAID: EPI_ISL_13777657) and BA.5.2 (GISAID: EPI_ISL_13777658) were isolated from laboratory-confirmed COVID-19 patients in Hong Kong. All variants of SARS-CoV-2 were cultured and titrated by plaque assays using VeroE6-TMPRSS2 cells. Sequences of all variants used in this study were confirmed with nanopore sequencing. In vivo and in vitro experiments with infectious SARS-CoV-2 were performed according to the approved standard operating procedures of the Biosafety Level 3 facility at Department of Microbiology, HKU.

Cell cultures

293T, and VeroE6 were maintained in Dulbecco's modified Eagle's medium (DMEM) (11965092, Gibco, Amarillo, Texas, USA) containing 10% fetal bovine serum, 100 units penicillin, and 100ug/ml streptomycin. Calu3 was maintained in DMEM/F12 (11320033, Gibco) containing 10% fetal bovine serum, 100 units penicillin, and 100ug/ml streptomycin. VeroE6-TMPRSS2 was cultured in DMEM supplemented with 10% fetal bovine serum, 100 units penicillin,100ug/ml streptomycin and 2% G418. All cells were cultured at 37 °C in an incubator with 5% CO_2. All cell lines used are routinely tested for mycoplasma and are maintained mycoplasma-free.

Virus infection in human nasal epithelial cell air-liquid interface (ALI) culture

The human nasal epithelial cells in air-liquid interface (ALI) culture were purchased from Epithelix (EP02MP, Epithelix, Switzerland) and maintained with MucilAir culture medium (EP04MM, Epithelix) until virus challenge. On the day of virus challenge, cells were washed with MucilAir culture medium to remove the apical mucin, followed by virus inoculation at the apical side at 2 multiplicity of infection (MOI). Cells were incubated for 2 h at 37 °C to allow virus entry. Residual inoculum was removed and washed away after incubation. Supernatants and cell lysates were harvested from the apical side for viral genome copy quantification with RNA extraction followed by one-step RT-qPCR and infectious virus titration with $TCID_{50}$ assays at the designated time points. For immunofluorescence staining, cells were fixed with neutral-buffered formalin followed by permeabilization with 0.1% Triton-X-100 (11332481001, Sigma–Aldrich, USA). The SARS-CoV-2 nucleocapsid protein and ciliated cells were detected with in-house rabbit anti-SARS-CoV-2 nucleocapsid serum[8,15] and mouse anti-beta-tubulin (T7941, Sigma–Aldrich, USA), respectively. Primary antibodies were visualized with Alexa Fluor 594-conjugated goat anti-mouse secondary antibody (A-11005, Thermo Fisher Scientific, USA) and Alexa Fluor 488-conjugated goat anti-rabbit secondary antibody (A-11034, Thermo Fisher Scientific), followed by mounting with ProLong™ Diamond Antifade Mountant with DAPI (P36962, Thermo Fisher Scientific). Images were acquired with a Carl Zeiss LSM880 confocal microscopy (Zeiss, USA). To acquire the monolayer image of hNECs, Z-stack was applied to capture each layer in the z-axis of hNECs. Orthogonal projection was used to stack the Z-stack into one image. Images were processed and analysed by ZEISS Zen (blue edition) software using the maximum intensity projection setting.

In vivo virus challenge in mice

Heterozygous K18-hACE2 C57BL/6J mice (2B6.Cg-Tg(K18-ACE2)2Prlmn/J) were obtained from The Jackson Laboratory. The C57BL/6J and A129 mice were obtained from the Centre for Comparative Medicine Research, the University of Hong Kong. The mice were kept in cages with individual ventilation under 65% humidity and an ambient temperature of 21–23 °C and a 12–12 h day–night cycle for housing and husbandry. Group sizes were chosen based on statistical power analysis and our prior experience in examining viral titres in SARS-CoV-2-infected K18-hACE2 transgenic and C57BL/6 mice. Gender- and age-matched mice were randomized into different experimental groups. For virus challenge in transgenic mice, female and male K18-hACE2 transgenic mice (aged 6–10 weeks) were anaesthetized with ketamine and xylazine, followed by intranasal inoculation with 20 μl per mouse of Omicron subvariants BA.1, BA.2, BA.2.12.1, BA.4.1 or BA.5.2 at 5000 PFU per mouse as we previously described.[17–19] For infection in the wildtype and A129 mice, female C57BL6/J (aged 6–8 weeks and aged 10–11 months) and female A129 mice (aged 6–8 weeks) were intranasally challenged with B.1.351, BA.2, BA.4.1 or BA.5.2 at 1×10^5 PFU. Mice were euthanized at 2 dpi. to collect nasal turbinate and lung tissues for virological assessment, histological examination and pathology scoring.

Histology and immunohistochemistry staining

Animal tissues were collected and fixed with 10% neutral-buffered formalin. Nasal turbinates were decalcified with 10% formic acid for 10 days before being processed with a semi-enclosed benchtop tissue processor (TP1020, Leica, Germany) and sectioned at 5 μm with the Leica RM2125 RTS benchtop microtome. Immunohistochemistry (IHC) staining was performed with in-house rabbit polyclonal anti-SARS-CoV-2 nucleocapsid protein antibodies (1:4000), followed by incubation with biotinylated goat anti-rabbit IgG (H + L) secondary antibody (1:500) (BA-1000, Vector laboratories,

USA). Color was developed with the VECTASTAIN® ABC-AP Kit (AK-5000) and VectorRed substrate kit (SK-5100, Vector Laboratories) according to the manufacturer's instructions. The nuclei were counterstained with Gill's haematoxylin before the tissue sections were mounted using the VectaMount permanent mounting medium (H-5000, Vector Laboratories). The nucleocapsid protein-covered area was quantified with the IHC Image analysis Toolbox in ImageJ (v.1.8.0_345). For H&E staining, tissue sections were stained with Gill's haematoxylin and eosin-Y. Images were acquired using the Olympus BX53 light microscope (Olympus Life Science, Japan). Three to four mice were sampled in each group (as specified in the figure legends) and four to six sections from each animal were used for histology analysis. To obtain the semiquantitative histology scoring, tissue sections were graded in a blinded manner according to the pathological changes in the nasal turbinate and lung tissues by an experienced pathologist as previously reported by us and others.[8,20]

In vivo *competition assay*

6-to-8-week-old female K18-hACE2 transgenic mice were intranasally challenged with mixture of BA.2 and BA.5.2 or BA.4.1 and BA.5.2 at 1:1 ratio based on their infectious viral tires at 5000 PFU of each virus. Mice were euthanized at 2 dpi. to collect nasal turbinate for RNA extraction with the RNeasy Mini kit (74106, Qiagen, MD, USA) and first strand cDNA synthesis using Transcriptor First Strand cDNA Synthesis Kit (04897030001, Roche, USA). The viral genome was amplified using Q5® High-Fidelity DNA Polymerase (M0491L, New England Biolabs, USA) with ARTIC network nCoV-2019 primers v4 (Integrated DNA Technologies, USA). The PCR amplicons were purified with SPRIselect beads (B23319, Beckman Coulter, USA) and quantified with Qubit Fluorometer (Thermo Fisher Scientific). The Illumina libraries were prepared using the KAPA HyperPrep Kit (KK8505, Roche Applied Science, Penzberg, Germany) using 100 ng as input following the manufacture protocol with double-sided size selection to select adapter ligated libraries with the size range 300–750 bp. PCR was performed for library enrichment followed by purification using AMPure XP beads (A63882, Beckman Coulter). The enriched libraries were validated using gel electrophoresis, Qubit and qPCR for quality control analysis. The libraries were denatured and diluted to optimal concentration prior sequencing on the Illumina MiSeq System using the MiSeq Reagent Kit v3 (600-cycle) (Illumina, San Diego, USA) for paired-end sequencing (PE301). The output fastq files were subjected to adapter removal using FASTP. The pair end reads were then combined into one read using Paired-End reAd merger (PEAR). Then, the assembled reads were filtered by Quality by FASTP by retaining reads of average Q score of 30, removing reads with at least 10% unqualified bases and length shorter than 300. The PCR primers were trimmed from the front and the end of each read. Pairwise alignments were performed between the BA.2 (GISAID: EPI_ISL_9845731) and BA.5.2 (GISAID: EPI_ISL_13777658) and between BA.4.1 (GISAID: EPI_ISL_13777657) and BA.5.2 genome sequence using SnapGene (v.3.2.1). Single nucleotide polymorphism (SNP) sites between the pair of genomes were extracted using SNP-SITES (v.2.5.1). Clean reads were mapped to the BA.2 and BA.4.1 genome for the competition assay between BA.2 and BA.5.2 and that between BA.4.1 and BA.5.2, respectively using BWA MEM (v.0.7.17) with default setting. The coverage statistics of both comparisons were retrieved from the BAM files with PYSAMSTATS (v.1.1.2) (https://github.com/alimanfoo/pysamstats). The abundance of BA.2, BA.4.1 and BA.5.2 was calculated based on the ratio of reads containing the variant-specific SNPs.

Infectious virus titration by $TCID_{50}$ assays and plaque assays

To quantify infectious viral titre with $TCID_{50}$ assays, nasal turbinates and lung tissues harvested from infected mice were homogenized in DMEM with Tissue Lyzer II (Qiagen) and clarified supernatants were 10-fold serially diluted and inoculated to monolayered VeroE6-TMPRSS2 cells. Supernatant samples from cells infected with SARS-CoV-2 WT, Delta, BA.1, BA.2, BA.2.12.1, BA.4.1 or BA.5.2 were harvested and 10-fold serially diluted before inoculated onto VeroE6-TMPRSS2 cells. Cytopathic effect (CPE) was observed at five days post infection for the quantification of the median tissue culture infectious dose. To compare the plaque size developed by SARS-CoV-2 WT, Omicron BA.1, BA.2, BA.2.12.1, BA.4.1 or BA.5.2, monolayer of VeroE6-TMPRSS2 cells in 12-well plate were challenged with different virus strains at 40 PFU/well. After 2 h infection, the cells were covered with 1% low-melting agarose in DMEM with 1% FBS for following incubation. The infected plates were fixed with 4% paraformaldehyde at 1, 2, 3, 4, or 5 dpi, followed by staining with 0.5% crystal violet in 25% ethanol/distilled water for plaque visualization. The diameter of plaques was measured by Adobe Photoshop CC software (v. 2018).

Cell viability assays

VeroE6-TMPRSS2 cells were infected with SARS-CoV-2 WT, Delta, BA.1, BA.2, BA.2.12.1, BA.4.1 or BA.5.2 at 0.1 MOI. Cell viability was quantified by CellTiter-Glo luminescent cell viability assay kit (G7573, Promega, WI, USA), following manufacturer's manual with the EnSight Multimode Microplate Reader (Perkin Elmer, USA) at the designated time points.

Package of SARS-CoV-2-spike pseudoviruses and pseudovirus entry assays

SARS-CoV-2-spike pseudoviruses were packaged as previously described.[8,21,22] Briefly, 293T cells were

transfected with different spikes with Lipofectamine 3000 (L3000-015, Thermo Fisher Scientific). At 24 h post transfection, the cells were transduced with VSV-deltaG-firefly pseudotyped with VSV-G. At 2 h post transduction, the cells were washed three times with PBS and cultured in DMEM containing 1%FBS and anti-VSV-G (8G5F11) antibody (EB0010, kerafast, Boston, MA, USA). The pseudoviruses were then harvested at 16 h post transduction and titrated with $TCID_{50}$ assays. For pseudovirus entry assays, target cells were inoculated with pseudoviruses for 2 h and cultured in media containing 1% FBS for 24 h, before washed and lysed for detection of luciferase signal with a luciferase assay system (E1501, Promega, Madison, WI, USA) according to manufacturer's instructions. All SARS-CoV-2 spike plasmids were obtained from GenScript (Nanjing, China).

RNA extraction and real-time reverse-transcription polymerase chain reaction

Viral RNA was extracted from infected cells using QIAsymphony RNA Kit (931636, Qiagen). Viral RNA of supernatants collected from infected cells was extracted using QIAamp Viral RNA Mini Kit (52906, Qiagen). Viral RNA from mice lung and nasal turbinate samples were extracted with the RNeasy Mini kit (74106, Qiagen). After RNA extraction, qRT-PCR was performed using QuantiNova Probe RT-PCR Kit (208354, Qiagen) or QuantiNova SYBR Green RT-PCR Kit (208154, Qiagen) with the LightCycler 480 Real-Time PCR System (Roche). The primer and probe sequences are available upon request.

Protease inhibitor treatment assay

The serine protease inhibitor, camostat (HY-13512), and the cysteine protease inhibitor, E64D (HY-100229), were purchased from MedChemExpress (Monmouth Junction, NJ, USA). VeroE6-TMPRSS2 cells were treated with DMSO, camostat, or E64D at concentration of 50 μM for 2 h before pseudovirus transduction. At 24 hpi, the cell lysates were lysed for detection of luciferase signal. The DMSO-treated cells transduced with pseudovirus carrying the same spike served as the control. Luciferase readings from the inhibitor-treated cells were normalized with the mock-treated controls. For protease inhibitor treatment on Calu3 and VeroE6 cells, Calu3 and VeroE6 cells were infected with the indicated Omicron sublineages at 0.5 MOI or 0.1 MOI after treatment with DMSO, camostat, or E64D at 25 μM for 2 h. At 24 hpi, virus infected cells were lysed for detection of viral sgE gene copies. The human nasal epithelial cells were infected with the indicated Omicron sublineages at 2 MOI after treatment with DMSO, camostat, or E64D at 10 μM for 2 h. At 72 hpi, supernatants were lysed for detection of viral RdRp gene copies.

Western blot analysis of spike cleavage

293T cells were transfected with spike plasmids of SARS-CoV-2 WT (614G), BA.1, BA.2, BA.2.12.1, BA.4/5 and S_1/S_2Del. For infection experiment, VeroE6 cells were challenged with SARS-CoV-2 WT, BA.1, BA.2 or BA.5.2 at 2 MOI. Cell lysates were harvested in RIPA buffer (89901, Thermo Fisher Scientific) at 24 h post transfection or infection for Western blot analysis. The membranes were blocked with 5% milk for 2h at room temperature and incubated with a rabbit anti-SARS-CoV-2 spike S2 antibody (40590-T62, Sino Biological, China) at 4 °C for overnight incubation, followed by detection with horseradish peroxidase (HRP) conjugated secondary antibodies (31460, Thermo Fisher Scientific) for 1h at room temperature. The signal was developed using SuperSignal West Pico PLUS Chemiluminescent Substrate (34580, Thermo Scientific) and detected using Alliance Imager apparatus (Uvitec, Cambridge, UK). β-actin was detected with a β-actin antibody (clone AC-74, A5316, Sigma–Aldrich) (1:5000).

Cell-cell fusion assay

293T cells were co-transfected with different SARS-CoV-2 spike plasmids with GFP1-10 plasmid (cat#68715, Addgene, USA) as effector cells. Another population of 293T cells was co-transfected with ACE2, TMPRSS2, and GFP11 (cat#68716, Addgene) as target cells. After 24 h post-transfection, the effector and target cells were digested by EDTA–Trypsin (25200-072, Gibco) and mixed at a 1:1 ratio. The mixed cells were co-cultured at a 37 °C incubator for another 24 h. The mixed cells were fixed in 10% formalin and then permeabilized with 0.1% Triton-X100 (Sigma, USA) at room temperature. The antifade mounting medium with 4′,6-Diamidino-2-Phenylindole, Dihydrochloride (DAPI, H-1200, Vector Laboratories) was used for mounting and DAPI staining. Images were taken with the Olympus BX73 fluorescence microscope (Olympus Life Science, Tokyo, Japan). The fusion area of images was quantified by ImageJ (v.1.8.0_345).

Ordinal logistic regression (OLR) of lung pathology score over time

Ordinal logistic regression (OLR) was used to model the lung pathology of K18-hACE2 mice infected by BA.1, BA.2, BA.2.12.1, BA.4.1, or BA.5.2 over time. The peak count date of Omicron sublineages was retrieved from the SARS-CoV-2 PANGO lineage online tool (https://cov-lineages.org/).[23] The correlation between the peak count date of each Omicron sublineage since COVID-19 outbreak and the lung pathology score was fitted to the OLR model with the R (v. 4.1.2) package MASS.

Ethics

The use of animals was approved by the Committee on the Use of Live Animals in Teaching and Research of

The University of Hong Kong under CULATR 22-139, 5440-20 and 5193-19. Experiment procedures have complied with the approved operation protocol.

Statistical analysis

Statistical comparison between two experimental groups were performed with unpaired two-tailed Student's *t*-test. Comparison between three or more experimental groups was performed with one-way or two-way ANOVA. Differences were considered statistically significant when $p < 0.05$. Data analysis was performed with GraphPad Prism 8.0.

Role of funders

All donors and funding sources had no role in the study design, data collection, analysis, interpretation, or writing of the manuscript.

Results

Comparative virological features of Omicron BA.1, BA.2, BA.4, and BA.5 sublineages

Over the past year, Omicron has continued to prevail as the dominant SARS-CoV-2 VOC worldwide. Among the emerged Omicron sublineages, BA.1, BA.2, BA.5, and their related sublineages resulted in the largest waves of infections (Fig. 1A). To perform in parallel comparison on the virological features of Omicron sublineages, we propagated the clinical isolates of BA.1,[8] BA.2,[15] BA.2.12.1, BA.4.1, and BA.5.2 in VeroE6-TMPRSS2 cells. BA.2.12.1 spike differs from BA.2 spike at L452Q and S704L. BA.4 and BA.5 share the same spike sequence, which differs from BA.2 spike at 69-70del, L452R, F486V, and R493Q. Our BA.4.1 isolate contains a V3G substitution in the signal peptide region and a H146Q substitution when compared to BA.4 spike. BA.5.2 and BA.5.2 related sublineages (BA.5.2.*) are the most dominant BA.5 related sublineages (Fig. 1A). BA5.2 shares the same spike sequence with BA.4 and BA.5 (Fig. 1B).

To compare the replication kinetics of different sublineages, we first infected Calu3 and VeroE6 cells with SARS-CoV-2 wildtype (WT), Delta, BA.1, BA.2, BA.2.12.1, BA.4.1, or BA.5.2 and harvested samples at different time points post infection. We assessed virus replication in cell lysates by quantification of subgenomic envelope (E) gene expression, which is a replication intermediate of SARS-CoV-2. In parallel, we quantified the level of infectious virus particles in the supernatants with 50% tissue culture infectious dose ($TCID_{50}$) assays. Our results demonstrated that all five Omicron sublineages replicated less efficiently in Calu3 cells when compared to that of WT and Delta. Among the Omicron sublineages, BA.5.2 replicated to the highest level in Calu3 cells, which was statistically different in infectious titre than that of BA.1 and BA.2.12.1 at 48 h post infection (hpi) (Fig. 1C). In VeroE6 cells, BA.5.2 infection generated higher infectious titre than that of Delta, BA.1, BA.2, BA.2.12.1, BA.4.1, and were comparable to that of WT (Fig. 1D). In keeping with its better replication, BA.5.2 infection resulted in lower cell viability in VeroE6-TMPRSS2 cells when compared to Delta, BA.1, BA.2, BA.2.12.1, and BA.4.1 at 30 and 36 hpi, while WT remained as the most cytopathic SARS-CoV-2 strain evaluated (Fig. 1E).

Next, we assessed the virological features of Omicron spikes. We found that cleavage of BA.1 and BA.2 spike at S_1/S_2 in the infected cells were less efficient than WT (D614G) (Fig. 2A), in keeping with previous studies from us and others.[7–9,15,21,24] Interestingly, cleavage of BA.5 spike was more efficient than that of BA.1 and BA.2 (Fig. 2A). To further dissect spike cleavage irrespective of non-spike viral proteins, we transfected 293T cells with spike expression plasmid of WT (D614G), BA.1, BA.2, BA.2.12.1, BA.4/5, and S_1/S_2Del (a WT spike mutant with deletions flanking the S_1/S_2 site) as a negative control,[25] and harvested cell lysates at 24 h post transfection to detect spike cleavage. Consistent with the observations in infected cells, we showed that BA.1, BA.2, and S_1/S_2Del spikes were less readily cleaved at S_1/S_2 than WT (D614G). While the cleavage of BA.2.12.1 spike was highly comparable with that of BA.2 spike, the cleavage of BA.4/5 spike was significantly more efficient than that of BA.2 ($P = 0.0396$), and was comparable with that of WT (D614G) ($P = 0.4321$) (Fig. 2B and C). In parallel, we analyzed spike-mediated cell-cell fusion in 293T cells using the split GFP fusion assays. In line with the spike cleavage results, BA.4/5 spike most efficiently mediated cell-cell fusion among the evaluated Omicron sublineages, and induced a comparable level of cell-cell fusion compared with that of WT (D614G) ($P = 0.3379$) (Fig. 2D and E). We next infected VeroE6-TMPRSS2 cells with WT, BA.1, BA.2, BA.2.12.1, BA.4.1, and BA.5.2, and quantified plaque formation at different time points post infection. We found that BA.5.2 infection resulted in the largest plaques among the evaluated Omicron sublineages on 5 days post infection, followed by BA.1. However, plaques formed upon WT infection remained significantly larger than that of BA.5.2 at 2 to 5 dpi (Fig. 2F and G). The more efficient spike cleavage at S_1/S_2 suggests that BA.4/5 may be more efficient in transmembrane serine protease 2 (TMPRSS2)-mediated entry. However, in pseudovirus entry assays, we found that the efficiency of TMPRSS2 usage by BA.4/5 pseudoviruses was similar to that of BA.2 pseudoviruses, and lower than that of WT (D614G) ($P < 0.0001$) and BA.1 pseudoviruses ($P = 0.0002$) (Fig. 2H). This observation agreed with results obtained in pseudovirus entry assays in the presence of camostat (pan-serine protease inhibitor), which demonstrated inefficient inhibition of BA.4/5 pseudovirus entry with camostat in VeroE6-TMPRSS2 cells (Fig. 2I). In contrast, BA.4/5 pseudovirus entry was more efficiently inhibited by E64D (pan-cysteine protease inhibitor) when compared to WT (D614G),

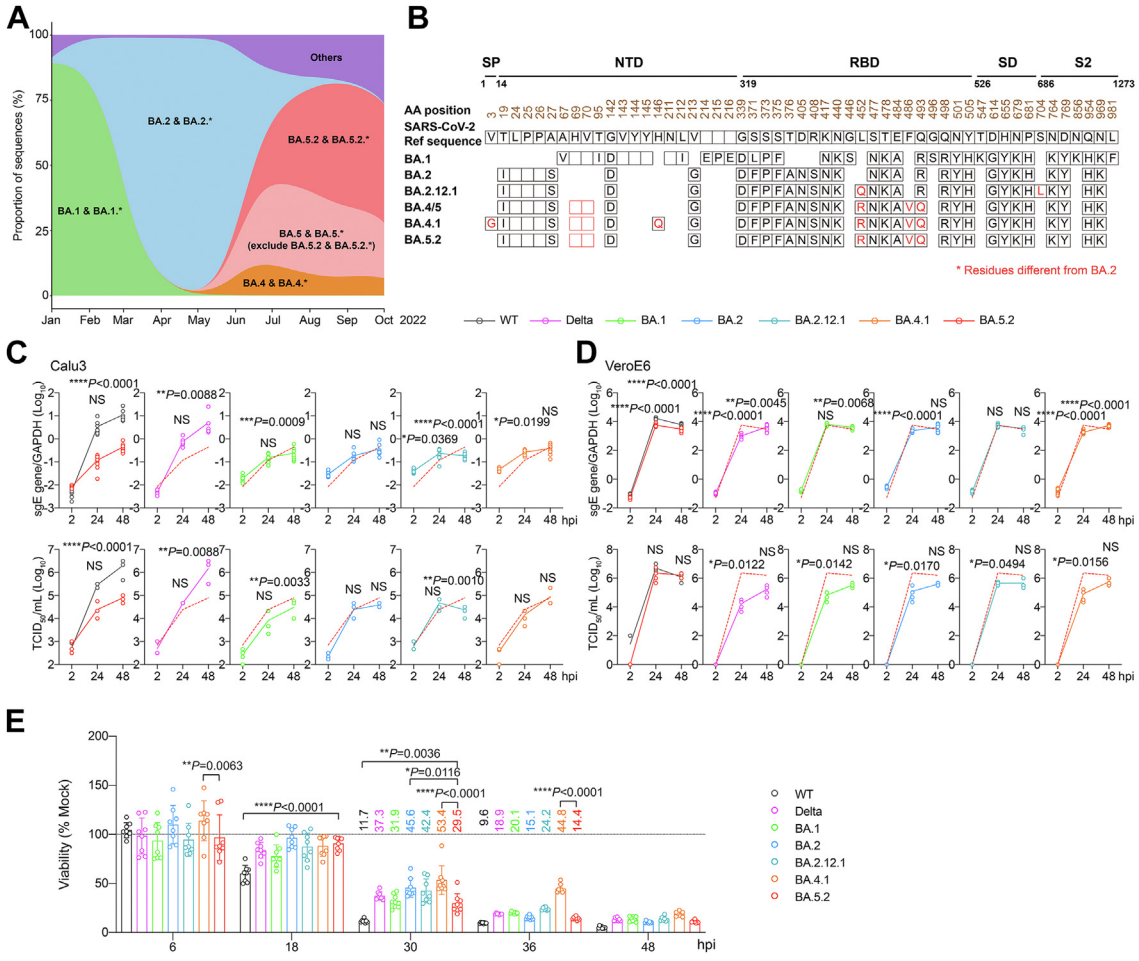

Fig. 1: **Virus replication kinetics of Omicron sublineages.** (**A**) The change in proportion of the genome sequences of SARS-CoV-2 Omicron sublineages deposited in GISAID from January 2022 to October 2022. The x-axis indicated the sequence collection date. The y-axis indicated the proportion of the SARS-CoV-2 Omicron sublineage sequences. (**B**) Amino-acid sequence alignment of SARS-CoV-2 reference strain Wuhan-hu-1, BA.1, BA.2, BA.2.12.1, BA.4, BA.4.1, BA.5, and BA.5.2 spike. Amino acid positions are designated based on SARS-CoV-2 reference strain. (**C and D**) Cells were challenged with SARS-CoV-2 WT, Delta, BA.1, BA.2, BA.2.12.1, BA.4.1 or BA.5.2 at 0.5 MOI (for Calu3) (**C**) or 0.1 MOI (VeroE6) (**D**). Cell lysates were harvested at the designated time points for quantification of the subgenomic RNA of the envelope (sgE) gene (n = 8). Infectious viral particles in supernatant samples were titrated with $TCID_{50}$ assays (n = 4). (**E**) Cell viability of VeroE6-TMPRSS2 cells infected with WT, Delta, BA.1, BA.2, BA.2.12.1, BA.4.1 or BA.5.2 at 0.1 MOI was quantified at the designated time points (n = 8). Data represents mean ± SD from the indicated number of biological repeats. Statistical significances were determined using two way-ANOVA with Sidak's multiple comparisons test (**C–D**) or with Dunnett's multiple comparisons test (**E**). Data were obtained from three independent experiments. Each data point represents one biological repeat. * represented p < 0.05 and ** represented p < 0.01. *** represented p < 0.001, **** represented p < 0.0001. NS, not statistically significant; WT, wildtype SARS-CoV-2.

BA.1, and BA.2 pseudovirus, and was inhibited to a similar degree compared to S_1/S_2Del and S_1/S_2AAAA (a WT spike mutant with the S_1/S_2 PRRA motif changed to AAAA) (Fig. 2I). To verify the data obtained from using pseudoviruses, Calu3 and VeroE6 cells were pretreated with camostat or E64D, followed by infection with WT (D614G), BA.1, BA.2, BA2.12.1, BA.4.1, BA.5.2 and S_1/S_2Del. In keeping with the pseudovirus findings, BA.5.2 showed reduced sensitivity to camostat in Calu3 cells and increased sensitivity to E64D in VeroE6 cells when compared with WT and earlier Omicron sublineages (Fig. 2J).

Replication fitness of Omicron BA.1, BA.2, BA.4, and BA.5 sublineages in primary human nasal epithelial cells

Omicron sublineages robustly evade neutralization antibody responses, which in part explained their highly efficient transmission in the immunized or previously exposed populations.[1–3,5,6] Meanwhile, the replication

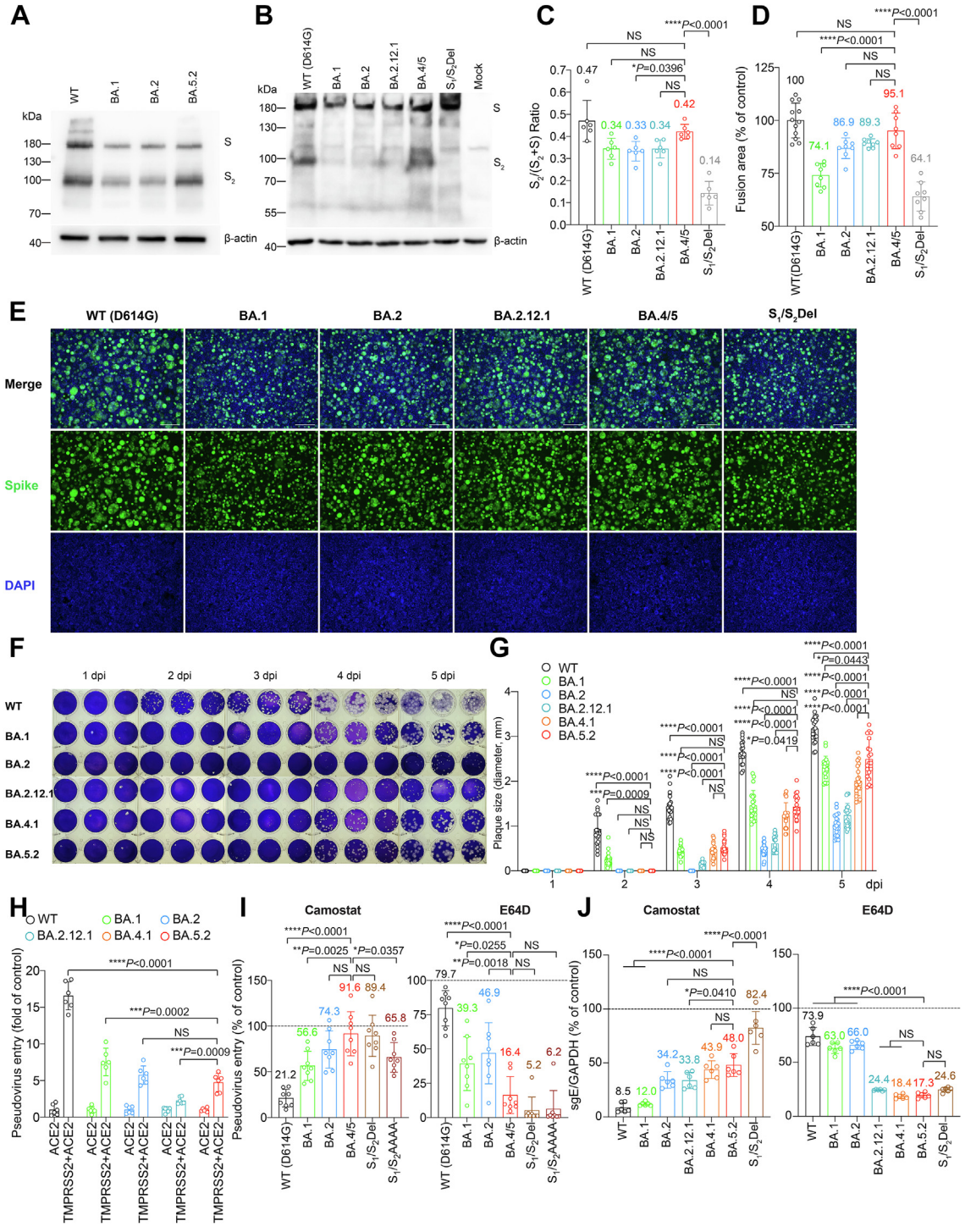

Fig. 2: **Virological features of Omicron sublineages in vitro.** (**A and B**) Representative image of spike cleavage in VeroE6 and 293T cells. (**A**) VeroE6 cells were infected with the indicated Omicron subvariants. (**B**) 293T cells were transfected with the indicated spike plasmids. Viral-infected or spike-transfected cell lysates were harvested at 24 hpi. for detection of SARS-CoV-2 spike cleavage with Western blotting using an anti-spike S2 antibody. Representative image of spike was shown with β-actin added as a sample processing control. Spike and β-actin were run on different gels and detected on different membranes. The experiment was repeated six times independently with similar results. (**C**) The cleavage ratio of spike proteins from six independent experiments in (**B**) was quantified by ImageJ. (**D**) Representative images of spike-mediated cell-cell fusion. 293T cells (effectors cells) were co-transfected with the indicated spike with GFP1-10, and were co-cultured with 293T cells co-

capacity of Omicron sublineages at the human nasal cavity, which may similarly play a role in their transmissibility, has not been thoroughly investigated. To this end, we sought to assess the replication fitness of SARS-CoV-2 WT, BA.1, BA.2, BA.4.1, or BA.5.2 in primary human nasal epithelial cells (hNECs). We first showed that the respiratory tract cell type markers for basal cells (P63, CK5), ciliated cells (FOXJ1, SNTN), and club cells (CC10) are significantly upregulated in the hNECs than that of lung epithelial Calu3 cells (Fig. 3A). In addition, we evaluated the expression of nasal markers (FOXG1, PAX7, SIX3) in the hNECs, and found that they are more highly expressed than that in Calu3 cells (Fig. 3B), suggesting that the compartment-specific gene expression profile of the hNECs is consistent with the human nasal epithelium as previously reported in single-cell sequencing analysis.[26] In parallel, we found that hNECs expressed SARS-CoV-2 entry factors (ACE2, TMPRSS2, cathepsin L, cathepsin B, and furin) at significantly higher levels than Calu3 cells (Fig. 3C). SARS-CoV-2 entry in hNECs predominantly occurred through the TMPRSS2-mediated plasma membrane pathway since SARS-CoV-2 entry was more readily inhibited by camostat than E64D (Fig. 3D). Upon virus infection, we harvested supernatants at 2, 24, 48, and 72 hpi and quantified the level of infectious virus production with $TCID_{50}$ assays. We found that while all Omicron sublineages replicated more efficiently than that of WT, BA.5.2 demonstrated the highest level of replication among all Omicron sublineages. At 48 hpi, BA.5.2 produced 27.0-folds ($P < 0.0001$), 4.9-folds ($P < 0.0001$), and 2.2-folds ($P = 0.0095$) higher infectious titre than that of WT, BA.1, and BA.2, respectively, and was comparable with that of BA.4.1. At 72 hpi, BA.5.2 produced 10.0-folds ($P < 0.0001$), 2.4-folds ($P = 0.0140$), 3.0-folds ($P = 0.0217$), and 1.7-fold ($P = 0.8277$) higher infectious titre than that of WT, BA.1, BA.2, and BA.4.1, respectively (Fig. 3E). Intriguingly, there is a trend of increasing fitness of SARS-CoV-2 replication in the hNECs, which was also evidenced by quantification of the RdRp gene in the supernatant samples and subgenomic E gene in the cell lysate samples at 72 hpi (Fig. 3F and G). In the cell lysates, the subgenomic E gene level upon BA.5.2 infection was 237.7-folds ($P = 0.0007$), 3.5-folds ($P = 0.0069$), 2.3-folds ($P = 0.0278$), and 1.8-fold ($P = 0.0787$) higher than that of WT, BA.1, BA.2, and BA.4.1, respectively (Fig. 3G). We further evaluated the antigen expression of WT-, BA.1-, BA.2-, BA.4.1-, and BA.5.2-infected hNECs by immunofluorescence staining at 24 hpi. Our data indicated that while all Omicron sublineages could target ACCTUB + ciliated cells in the hNECs, the highest number of nucleocapsid (N)-expressing cells were detected in BA.5.2-infected samples, followed by BA.4.1, BA.2, and BA.1 in a descending order (Fig. 3H). In contrast, N-expressing ciliated cells were scarcely detected in the WT-infected hNECs (Fig. 3H). Together, these results revealed that all Omicron sublineages replicated significantly more robustly than WT in hNECs. In addition, the sequentially emerged Omicron sublineages are gaining further replication fitness in the hNECs.

Replication and pathogenicity of Omicron BA.1, BA.2, BA.4, and BA.5 sublineages in K18-hACE2 transgenic mice

To investigate the in vivo replication fitness of the dominant Omicron sublineages at different stages of the Omicron wave, we intranasally challenged 6-to-10-week-old K18-hACE2 transgenic mice with 5000 PFU of BA.1, BA.2, BA.2.12.1, BA.4.1 or BA.5.2, and euthanized the infected mice at 2 dpi to collect nasal turbinates and lung tissues for virological assessment (Fig. 4A–D). In the nasal turbinate samples, BA.5.2 infection resulted in the highest viral sgE gene copies, which was

transfected with hACE2, TMPRSS2, and GFP11 (target cells) at a 1:1 ratio. The co-cultured cells were fixed with 4% PFA, permeabilized with 0.1% Triton-X100, and stained with DAPI. Representative images were from four independent experiments with similar results. (**E**) The fusion area was quantified by ImageJ. Results were normalized with the SARS-CoV-2-WT (D614G) group. (**F**) Plaque assay images of SARS-CoV-2 WT, BA.1, BA.2, BA.2.12.1, BA.4.1 and BA.5.2 in VeroE6-TMPRSS2 cells. VeroE6-TMPRSS2 cells were challenged with SARS-CoV-2 WT, BA.1, BA.2, BA.2.12.1, BA.4.1 and BA.5. The infected cells were fixed with 4% paraformaldehyde at the designated time points and stained with crystal violet ($n = 3$). The experiment was repeated three times independently with similar results. Each well represents one biological repeat. (**G**) Plaque diameters at the indicated time points were measured by Adobe Photoshop ($n = 20$). (**H**) 293T cells were transfected with hACE2 or co-transfected with hACE2 and TMPRSS2, followed by transduction with pseudoviruses expressing the spike of SARS-CoV-2 WT (D614G), BA.1, BA.2, BA.2.12.1, BA.4/5 at 24 h post-transfection. Pseudovirus entry was quantified by measuring the luciferase signal ($n = 6$). Fold change in the luciferase signal was normalized to the mean luciferase readouts of cells with only hACE2 overexpression. (**I**) VeroE6-TMPRSS2 cells were pre-treated with 50 μM camostat (left panel) and E64D (right panel) for 2 h followed by transduction with pseudoviruses expressing the spike of SARS-CoV-2 WT (D614G), BA.1, BA.2, BA.4/5, S_1/S_2Del, S_1/S_2AAAA at 24 h post-transfection. Pseudovirus entry was quantified by measuring the luciferase signal ($n = 8$). The luciferase signal was normalized to the mean luciferase readouts of cells treated with DMSO. (**J**) Calu3 (left panel) and VeroE6 (right panel) cells were pre-treated with 25 μM camostat and E64D, respectively, for 2 h followed by challenge with authentic viruses SARS-CoV-2 WT, BA.1, BA.2, BA.2.12.1, BA.4.1, BA.5.2, SARS-CoV-2 S_1/S_2Del. Viral-infected cell lysates were harvested at 24 hpi for quantification of the subgenomic RNA of the envelope (sgE) gene ($n = 6$). Data represents mean ± SD from the indicated number of biological repeats. Statistical significance was determined with one-way ANOVA (**C, D, I, and J**) or two-way ANOVA (**G and H**). Data were obtained from three independent experiments. Each data point represents one biological repeat. * represented $p < 0.05$ and ** represented $p < 0.01$. *** represented $p < 0.001$, **** represented $p < 0.0001$. NS, not statistically significant. WT, wildtype SARS-CoV-2.

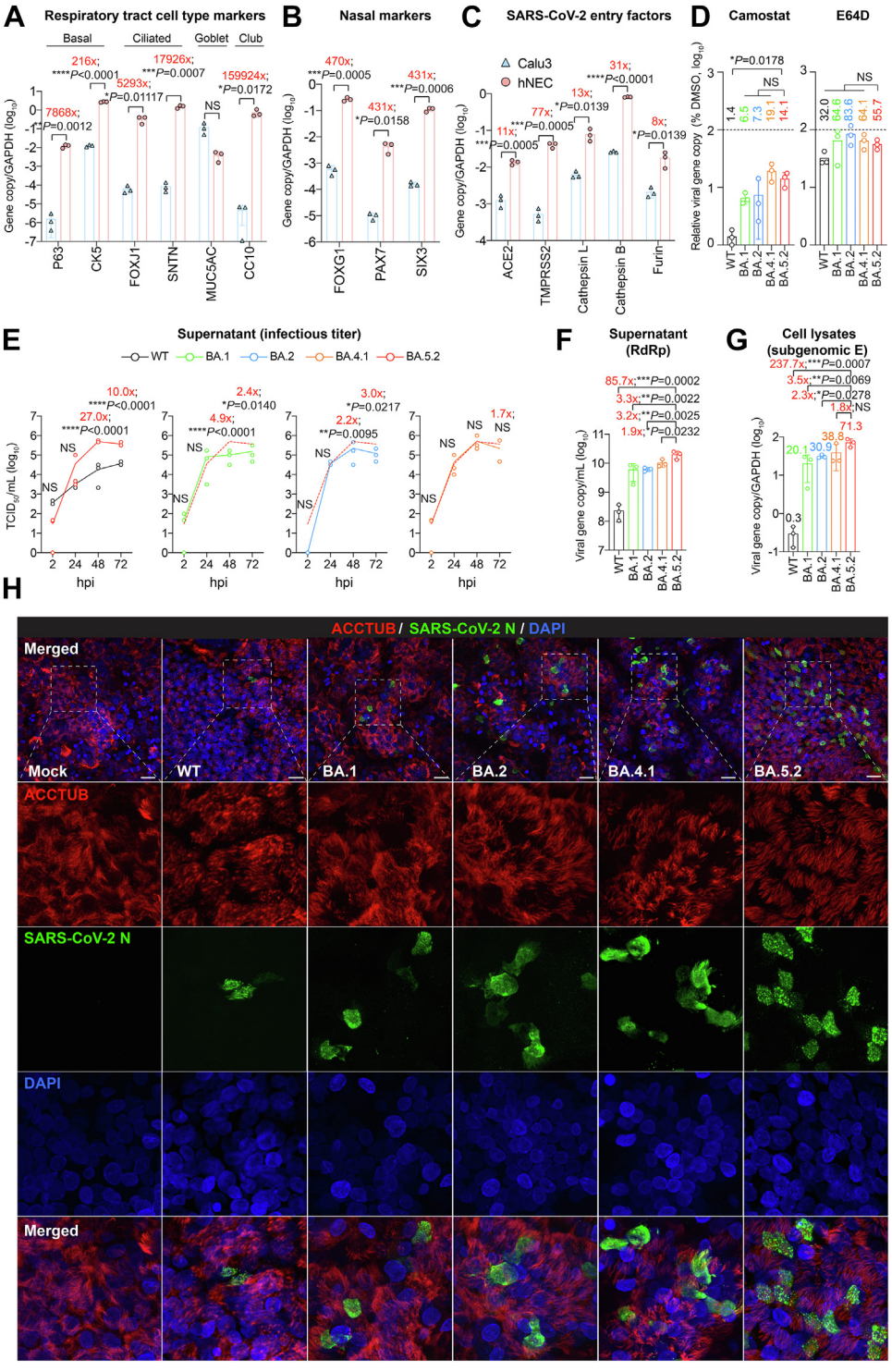

Fig. 3: **Virological assessment of Omicron BA.1, BA.2, BA.4.1, BA.5.2 in primary human nasal epithelial cells.** (**A**) Gene expression level of the respiratory tract epithelial cell markers in primary human nasal epithelial cells (hNECs) and Calu3 cells (n = 3). (**B**) Gene expression level of the nose-enriched markers in hNECs and Calu3 cells (n = 3). (**C**) Gene expression level of SARS-CoV-2 entry factors in hNECs and Calu3 cells (n = 3). (**D**) hNECs were pre-treated with 10 μM camostat (left panel) or E64D (right panel) for 2 h followed by SARS-CoV-2 WT, BA.1, BA.2, BA.4.1, or BA.5.2 infection at 2 MOI (n = 3). Supernatant samples were harvested at 72 hpi and the viral RdRp gene level was quantified with qRT-PCR. (**E–G**) hNECs were infected with BA.1, BA.2, BA.4.1, BA.5.2, or WT SARS-CoV-2 at 2 MOI (n = 3). Supernatants were harvested for

18.5- (P = 0.0273) and 10.5-folds (P = 0.0309) higher than that of BA.1 and BA.2, respectively (Fig. 4A). Consistently, the infectious viral titre of BA.5.2-infected mouse nasal turbinates were 7.7- (P = 0.0110) and 1.6-fold (P = 0.4480) higher than that of the BA.1- and BA.2-infected mouse nasal turbinates, respectively (Fig. 4C). We next assessed the replication of BA.5.2 in the lungs of the infected K18-hACE2 mice, and detected comparable RNA levels for BA.1, BA.2, and BA.5.2 (Fig. 4B). The mean infectious titre of BA.5.2 (0.9×10^5 PFU/g) in lungs of infected animals was slightly lower than that of BA.1 (1.4×10^5 PFU/g) and BA.2 (1.9×10^5 PFU/g), but did not reach statistical significance (Fig. 4D). To further characterize the viral antigen expression in vivo, we performed immunohistochemistry staining to detect the SARS-CoV-2 nucleocapsid (N) protein in nasal turbinates and lungs of the infected mice (Fig. 4E–H). In keeping with the virus burden findings in the nasal turbinate, N protein was most abundantly detected in the nasal epithelium of BA.5.2-infected mice when compared to their counterparts infected with BA.1, BA.2, BA.2.12.1, or BA.4.1 (Fig. 4G). With quantification, the N protein-covered area in nasal turbinates of BA.5.2-infected mice was 7.5- (P = 0.0026) and 1.9-folds (P = 0.0179) higher than that of BA.1- and BA.2-infected mice, respectively (Fig. 4E). Consistent with the infectious titre results, N protein in the lungs of BA.5.2-infected mice (1.4%) was less readily detected when compared to those of BA.1- (2.3%) and BA.2-infected mice (2.1%) (Fig. 4F and H).

To investigate the pathogenicity caused by the Omicron sublineages, we performed comparative histopathological analysis with haematoxylin and eosin (H&E) staining on the nasal turbinate and lung tissues harvested at 2 dpi. We first examined the nasal turbinate tissues of BA.5.2-infected mice and found that the pathological changes were featured by extensive epithelium damage. Integrity of the epithelium lining was destroyed due to severe epithelial cell loss, while necrotic epithelial cell deposition and proteinaceous exudates were frequently identified in the nasal cavity (Fig. 5A). Similarly, significant epithelium desquamation and cell necrosis were also observed in the nasal turbinate of BA.2-infected mice (Fig. 5A). In contrast, scattered nasal epithelial cell loss was occasionally spotted in the nasal epithelium of BA.4.1-infected mice, while the nasal epithelium lining in BA.1- and BA.2.12.1-infected animals remained largely intact, with only a small amount of inflammatory cell infiltrates accompanied with proteinaceous exudates found in the nasal cavity (Fig. 5A). We adopted a semi-quantitative histopathological scoring system to describe the pathological findings as previously reported.[8] In the nasal turbinates, BA.5.2 infection contributed to the highest pathology scores, followed by BA.2 (Fig. 5B–D). The mean pathology score in the nasal turbinate of BA.5.2-infected mice was 5.0, which was higher than that of BA.2-infected mice (3.5) and BA.1-infected mice (0.5) (Fig. 5D). Next, we examined the histopathological changes in the lung tissues. In general, inflammation in the lung was mild among all Omicron sublineages examined. Localized inflammatory infiltration in the lamina propria, alveolar septa, and perivascular area was universally identified in all experimental groups (Fig. 5A). Semi-quantitative scoring identified a total lung pathology score of 0.8 in BA.5.2-infected mice, which was lower than that of BA.2-infected mice (2.0) and BA.1-infected mice (2.3) (Fig. 5E–H). We performed an ordinal logistic regression (OLR) based on the total lung pathology score and the peak count date of BA.1, BA.2, BA.2.12.1, BA.4.1, and BA.5.2, and found that the sequentially emerged Omicron sublineages are significantly declining in intrinsic lung pathology over time (β = –0.01361, P = 0.0399) (Fig. 5I). In comparison, lungs of the mock-infected littermates were absence of any identified pathological changes (Supplementary Fig. S1). Collectively, our histopathological findings corroborated with the virological assessment results and provided further evidence that the increasing replication fitness of Omicron sublineages in the nasal turbinates results in more severe pathological damage in the nasal epithelium, with BA.5.2 infection causes the most severe damage among all evaluated Omicron sublineages. In mouse lungs, Omicron sublineages are continuously attenuated and BA.5.2 resulted in milder pathology when compared to the previous dominant Omicron sublineages, BA.2 and BA.1.

Replication fitness of BA.2, BA.4 and BA.5 in K18-hACE2 transgenic mice

As evidenced by the more robust replication fitness of BA.5.2 over BA.2 and BA.4.1 in the nasal turbinates, we

titration of (**E**) infectious viral titres with $TCID_{50}$ assays at 2, 24, 48 and 72 hpi and quantification of (**F**) viral RdRp gene copies at 72 hpi. (**G**) Cell lysates were harvested at 72 hpi for quantification of viral subgenomic E gene (sgE) copies and were normalized with housekeeping gene GAPDH (n = 3). (**H**) hNECs infected with BA.1, BA.2, BA.4.1, BA.5.2, or WT SARS-CoV-2 at 2 MOI were fixed at 24 hpi for the visualization of ciliated cell marker beta-tubulin (red) and SARS-CoV-2 nucleocapsid protein (green) by immunofluorescence staining. Scale bar, 20 μm. Data were obtained from three independent experiments. Each data point represents one biological repeat. Data represent mean ± SD from the indicated number of biological repeats. Statistical significance was determined with multiple two-tailed Student's t-test (**A–C**), one-way ANOVA with Dunnett's multiple comparison tests (**D, F, and G**), and two-way ANOVA with Sidak's multiple comparison tests (**E**). *p < 0.05, **p < 0.01, ***p < 0.001, ****p < 0.0001. NS, not statistically significant. WT, wildtype SARS-CoV-2.

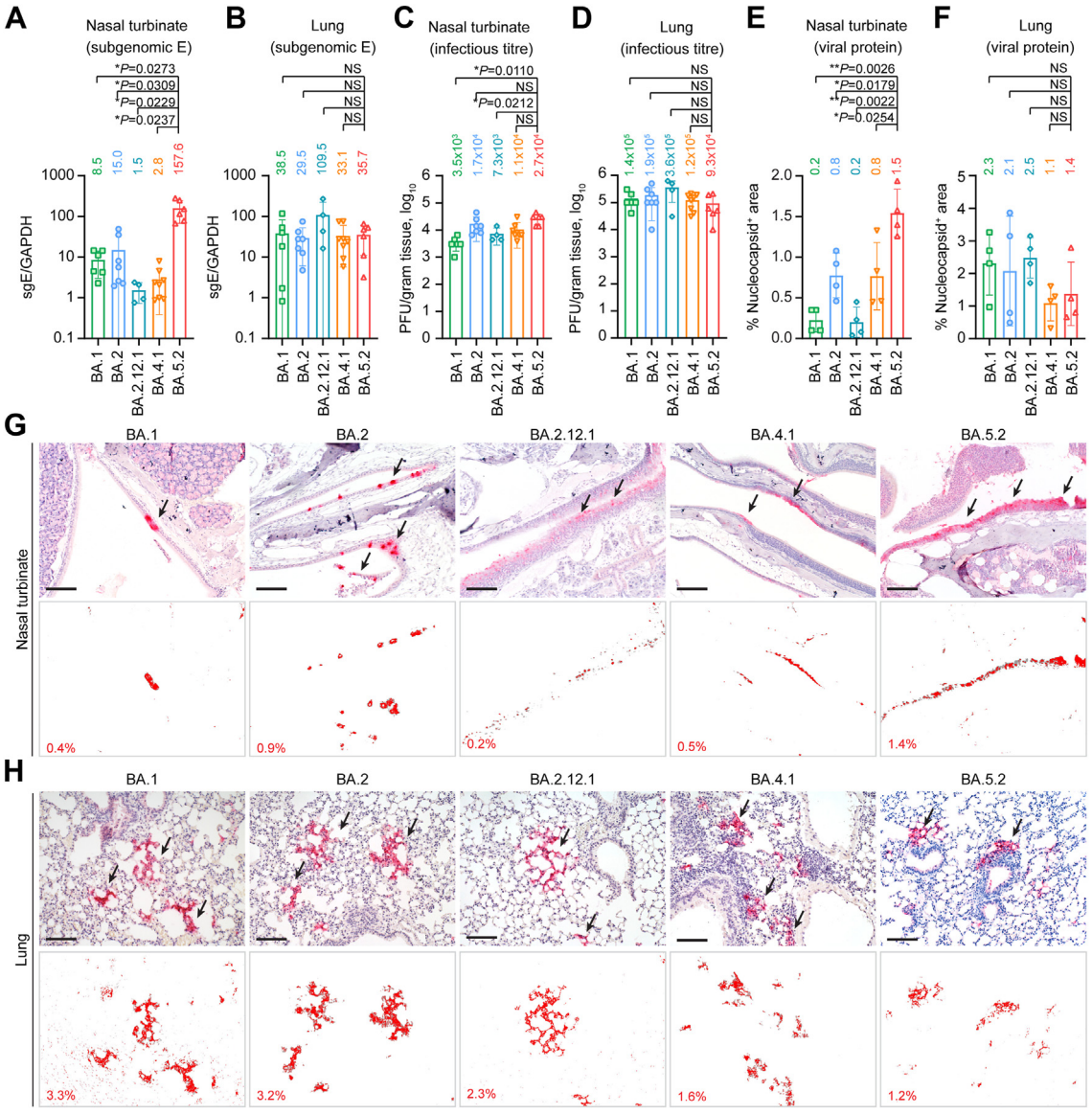

Fig. 4: **Virological assessment of Omicron BA.1, BA.2, BA.2.12.1, BA.4.1 and BA.5.2 in K18-hACE2 transgenic mice.** 6-to-10-week-old male and female K18-hACE2 transgenic mice were challenged with 5000 PFU Omicron subvariants BA.1 (n = 6), BA.2 (n = 7), BA.2.12.1 (n = 4), BA.4.1.2 (n = 8) and BA.5.2 (n = 6). Mice were euthanized at 2 dpi for collection of nasal turbinate and lung tissues for detection of viral burden and viral antigen expression. (**A and B**) Viral sgE copies were quantified with probe-specific RT-qPCR in the (**A**) nasal turbinate and (**B**) lung. (**C and D**) Infectious viral titres were quantified with plaque assays in the (**C**) nasal turbinate and (**D**) lung samples. (**E and F**) SARS-CoV-2 nucleocapsid protein in the (**E**) nasal turbinate and (**F**) lung was quantified with ImageJ. Four mice from each experiment group were used for viral antigen expression quantification. (**G and H**) Representative images of immunohistochemistry staining for the detection of SARS-CoV-2 nucleocapsid protein (red, indicated with arrows) in the (**G**) nasal turbinate and (**H**) lung. Scale bar, 100 μm. Data represent mean ± SD from the indicated number of biological repeats. Statistical significance was determined with Brown-Forsythe and Welch one-way ANOVA with Dunnett's T3 multiple comparisons tests (**A–F**). Data were obtained from three independent experiments. Each data point represents one biological repeat. Mean value for each experiment group were shown. *p < 0.05, **p < 0.01. NS, not statistically significant.

postulated that BA.5.2 might be able to outcompete BA.2 and BA.4.1 in the nasal turbinates of infected mice. To evaluate this hypothesis, we carried out competition assays between BA.5.2 and BA.2 by inoculating a mixture of the two viruses (each at 5000 PFU) to the K18-hACE2 mice. At 2dpi, we harvested nasal turbinate tissues for detection of the viral genome abundance with next generation sequencing

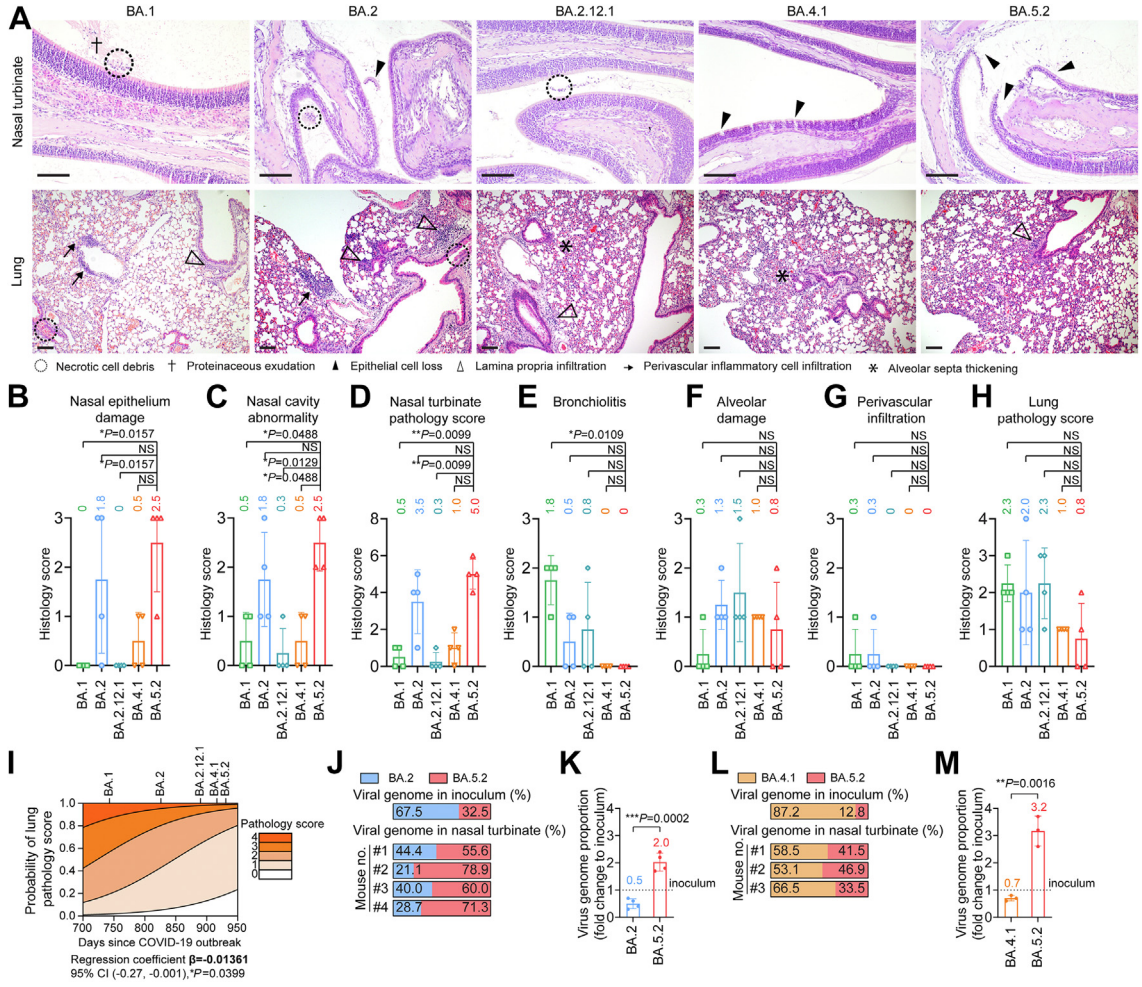

Fig. 5: **Pathogenicity and replication fitness of Omicron BA.1, BA.2, BA.2.12.1, BA.4.1 and BA.5.2 in K18-hACE2 transgenic mice.** (**A**) Representative images of H&E staining of the nasal turbinate and lung. Dashed circles, necrotic cell debris; closed arrowheads, epithelium desquamation; arrows, perivascular inflammatory cell infiltration; cross, proteinaceous exudation; open arrowheads, lamina propria infiltration; asterisk, alveolar septa thickening. Three sections were taken from each animal for immunochemistry analysis. Scale bar, 100 μm. (**B–D**) Semiquantitative analysis of the pathological changes in the nasal turbinate. (**B**) Nasal epithelium damage (0 = normal structure; 1 = mild epithelial cell loss; 2 = moderate epithelium desquamation; 3 = severe epithelium detachment) and (**C**) nasal cavity abnormality (necrotic epithelial cell debris, protein/fibrin deposition, and inflammatory cell infiltration each scored 1 point) were scored accordingly. (**D**) Pathology scores of the of the nasal turbinate were shown by adding the histological scores of nasal epithelium damage and abnormalities in the nasal cavity of each animal. (**E–H**) Semiquantitative analysis of the pathological changes in the lung. (**E**) Bronchiolitis (0 = normal structure; 1 = mild peribronchiolar infiltration; 2 = peribronchiolar infiltration plus epithelial cell death; 3 = score 2 plus intrabronchiolar wall infiltration and epithelium desquamation), (**F**) alveolar damage (0 = normal structure; 1 = alveolar wall thickening and congestion; 2 = focal alveolar space infiltration or exudation; 3 = diffused alveolar space infiltration or exudation or haemorrhage) and (**G**) perivascular infiltration (0 = normal structure; 1 = mild perivascular oedema or infiltration; 2 = vessel wall infiltration; 3 = severe endothelium infiltration) were scored accordingly. (**H**) Pathology scores of lungs were shown by adding the histological scores of bronchiolitis, alveolar damage, and perivascular infiltration in the lung of each animal. (**I**) Logistic regression based on the lung pathology scores presented in (**H**) and the peak count date of the indicated Omicron sublineages. Each sublineages were shown according to the individual peak count date proportionally since COVID-19 outbreak. Logistic regression coefficient (β), its 95% confidence interval (CI) and the p-value (P) were shown. (**J–M**) BA.2 and BA.5.2 or BA.4.1 and BA.5.2 were mixed at 1:1 ratio based on their infectious viral titres at 5000 PFU, followed by intranasal inoculation of the mixture into three to four 6-to-8-week-old female K18-hACE2 transgenic mice. Nasal turbinate was harvested at 2 dpi and subject to next generation sequencing (NGS) analysis. Proportion of viral genome copies of the nasal turbinate samples determined with NGS analysis were shown from the competition assay between (**J**) BA.2 and BA.5.2 (n = 4) and (**L**) BA.4.1 and BA.5.2 (n = 3). Viral genome abundance (**K**) between BA.2 and BA.5.2 (n = 4) and (**M**) between BA.4.1 and BA.5.2 (n = 3) was compared with that of the inoculum and shown in fold change. Data represent mean ± SD from the indicated number of biological repeats. Statistical significance was determined with Brown-Forsythe and Welch one-way ANOVA with Dunnett's T3 multiple comparisons tests (**B–H**) and two-tailed Student's t-tests (K and M). Data were obtained from three independent experiments. Each

(NGS) analysis. The NGS results indicated that BA.5.2 rapidly outcompeted BA.2 in the nasal turbinate of all four infected mice at as early as 2dpi (Fig. 5J). The mean virus genome proportion of BA.5.2 in the nasal turbinate samples increased to 2-folds when compared to that of the inoculum (32.5% in the inoculum vs 66.4% in harvested samples), while that of BA.2 was decreased to 0.5-fold (67.5% in the inoculum vs 33.6% in harvested samples) ($P = 0.0002$) (Fig. 5K). We next compared the viral fitness between BA.5.2 and BA.4.1, and showed that BA.5.2 similarly outcompeted BA.4.1 in the nasal turbinates of all three co-infected mice at 2 dpi (Fig. 5L). The mean virus genome abundance of BA.5.2 increased to 3.2-folds when compared to that of the inoculum while that of BA.4.1 diminished to 0.7-fold ($P = 0.0016$) (Fig. 5M). Thus, these results indicated that BA.5.2 demonstrated better replication fitness than BA.2 and BA.4.1 in the nasal turbinates of infected mice. Taken together, the nasal turbinate findings from K18-hACE2 mice agreed with results obtained from the hNECs, indicating that the Omicron sublineages are gaining replication fitness in the nasal epithelium of humans and mice, with BA.5.2 demonstrated the most robust replication capacity. Meanwhile, the trend is different in the lungs with BA.5.2 demonstrated lower antigen expression when compared with the previous dominant Omicron sublineages BA.1 and BA.2.

Replication fitness and pathogenicity of Omicron sublineages in young C57BL/6, A129, and aged C57BL/6 mice

Since Omicron sublineages carry the N501Y mutation in spikes that renders infectivity to wildtype (WT) mice (Supplementary Fig. S2),[27,28] we further infected young C57BL/6 mice (aged 6–8 weeks), aged C57BL/6 mice (aged 10–11 months), and the type I interferon receptor knockout A129 mice (aged 6–8 weeks) to investigate the differential replication and pathogenicity characteristics of Omicron sublineages between the immunocompromised and immunocompetent mouse models. We intranasally challenged the three animal models with 1×10^5 PFU of BA.2, BA.4.1 and BA.5.2 and measured viral burdens in the nasal turbinate and lung tissues at 2 dpi. Additionally, we used the N501Y-carrying B.1.351 (Beta) as a control, which was previously shown to be capable of infecting WT murines.[27] As expected, B.1.351 replicated at high levels in both nasal turbinates and lung tissues in all three mouse models (Fig. 6A and B). In the nasal turbinates of young C57BL/6 mice, while the replication of all evaluated Omicron sublineages was attenuated compared with B.1.351, the replication of BA.5.2 was significantly more efficient than that of BA.2 ($P = 0.0088$) (Fig. 6A), in keeping with our findings in K18-hACE2 mice. In the nasal turbinates of aged C57BL/6 mice, while the replication of Omicron BA.2 was attenuated compared with B.1.351, the replication of BA.5.2 was significantly more robust than that of BA.2 ($P = 0.0038$) and B.1.351 ($P = 0.0435$) (Fig. 6A). In the nasal turbinates of A129 mice, the replication of BA.5.2 was significantly more efficient than that of BA.2 but was lower than that of B.1.351, similar to the pattern observed in young C57BL/6 mice (Fig. 6A). Overall, the viral sgE copy in the nasal turbinates of BA.5.2-infected mice was 3.5- ($P = 0.0088$), 6.4- ($P = 0.0038$), and 5.7-folds ($P = 0.0038$) higher than that of BA.2 in young C57BL/6, aged C57BL/6, and A129 mice, respectively (Fig. 6A). In the lung tissues of young C57BL/6 mice, while BA.2 replication was reduced when compared to B.1.351, BA.5.2 replication was further attenuated by 12.9-folds when compared to BA.2 ($P = 0.0096$) (Fig. 6B). In contrast to the observation from young C57BL/6 mice, in the lung tissues of aged C57BL/6 mice and A129 mice, the replication of BA.5.2 was not attenuated when compared to BA.2 (Fig. 6B). We next determined the production of progeny viruses in lungs with plaque assays. Our data indicated that the infectious viral titre of BA.5.2 was 22-folds ($P = 0.0100$) lower in comparison to BA.2 in the lungs of young C57BL/6 mice (Fig. 6C). In lungs of aged C57BL/6 mice and A129 mice, the infectious viral titre of BA.5.2 was largely comparable with that of BA.2 (Fig. 6C). To evaluate the differences in viral antigen expression among the Omicron sublineages, we detected the abundance of viral N protein in lung tissues with immunohistochemistry staining. In corroboration with the virological assessment results, viral antigen expression in lungs of BA.5.2-infected young C57BL/6 mice were 19.3- ($P = 0.0163$) and 11.3-folds ($P = 0.0266$) lower than those of B.1.351 and BA.2, respectively. In contrast, viral N protein was expressed at comparable levels between BA.5.2 and BA.2 in the lungs of aged C57BL/6 mice and A129 mice (Fig. 6D and E).

In parallel, we assessed histopathological changes and corresponding pathology scores with formalin-fixed right lungs collected from the three infection models. We found that compared to mock infection which contributes to no pathological changes in mouse lungs (Supplementary Fig. S1), B.1.351 infection uniformly led to obvious pathological damages in the lungs of young C57BL/6, aged C57BL/6, and A129 mice at 2 dpi, including moderate to severe bronchiolitis (Fig. 7A and B), multifocal alveolar haemorrhage (Fig. 7A and C),

data point represents one biological repeat. Mean value for each experiment group were shown. *p < 0.05, **p < 0.01, ***p < 0.001. NS, not statistically significant.

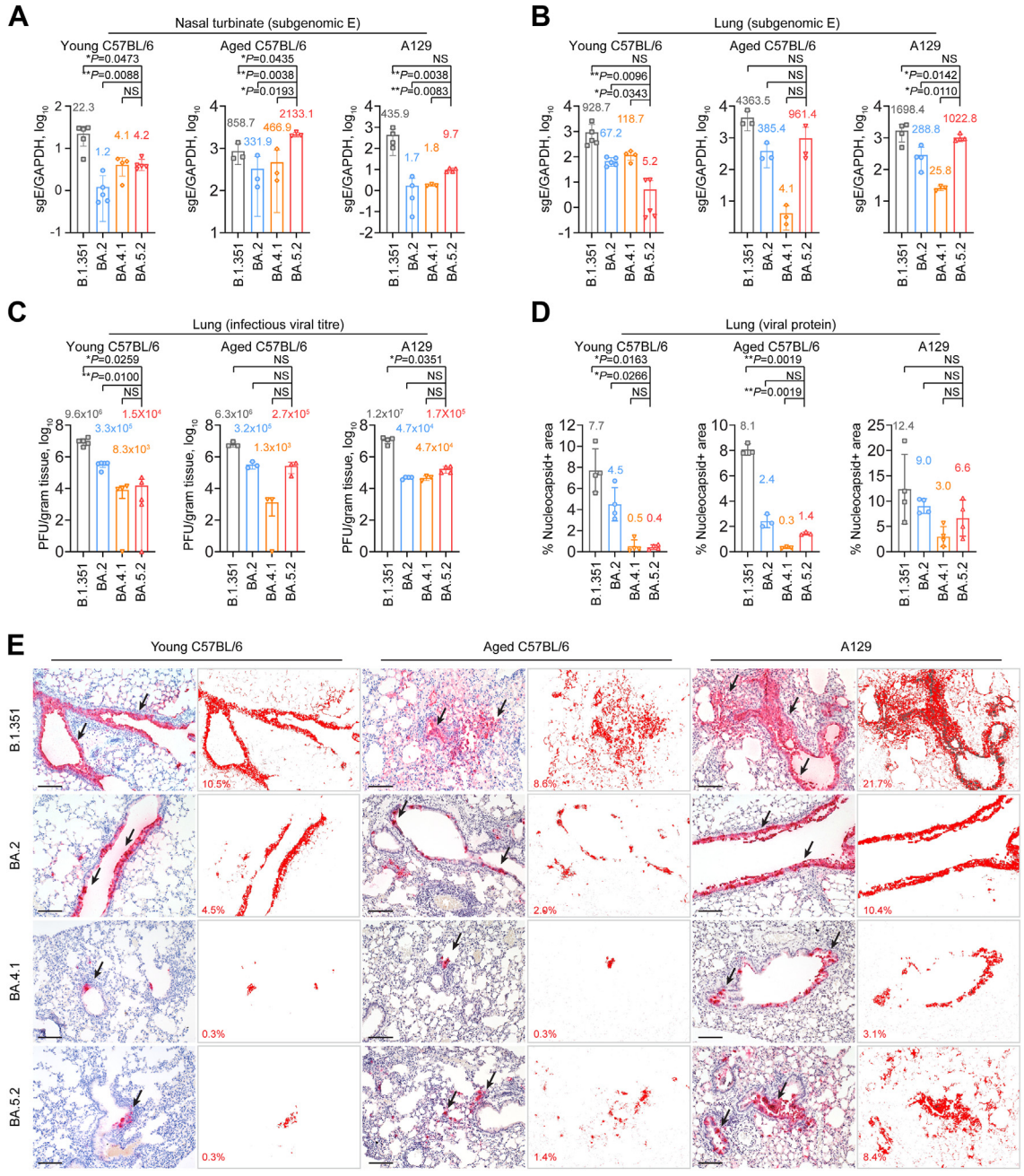

Fig. 6: **Virological assessment of Omicron BA.2, BA.4.1 and BA.5.2 in WT C57BL/6, aged C57BL/6, and A129 mice.** 6-to-8-week-old female C57BL/6 (n = 4 for BA.4.1; n = 5 for B.1.351, BA.2, and BA.5.2), 10-to-11-month old female C57BL/6 (n = 3 for B.1.351, BA.2, BA.4.1, and BA.5.2) and 6-to-8-week-old female A129 (n = 4 for B.1.351, BA.2, BA.4.1 and BA.5.2) mice were challenged with 1 × 10^5 PFU Omicron subvariants BA.2, BA.4.1, BA.5.2, or B.1.351 (Beta). Mice were euthanized at 2 dpi for collection of nasal turbinate and lung tissues for detection of viral burden and lung tissues for viral antigen expression. (**A and B**) Viral sgE copies in the (**A**) nasal turbinate and (**B**) lung were quantified with probe-specific RT-qPCR. (**C**) Infectious viral titres in the lungs were quantified with plaque assays. (**D**) Viral antigen expression in the lung was quantified with the SARS-CoV-2 nucleocapsid protein expression by ImageJ. Four mice from each experimental group were used for viral antigen expression quantification. (**E**) Representative images of immunohistochemistry staining for the detection of SARS-CoV-2 nucleocapsid protein (red, indicated with arrows) in the lung. The corresponding nucleocapsid protein positive area was quantified with ImageJ and shown. Three sections were taken from each animal for immunochemistry analysis. Scale bar, 100 μm. Data represent mean ± SD from the indicated number of biological repeats. Statistical significance was determined with Brown-Forsythe and Welch one-way ANOVA with Dunnett's T3 multiple comparisons test in (**A–D**). Data were obtained from three independent experiments. Each data point represents one biological repeat. *p < 0.05, **p < 0.01. NS, not statistically significant.

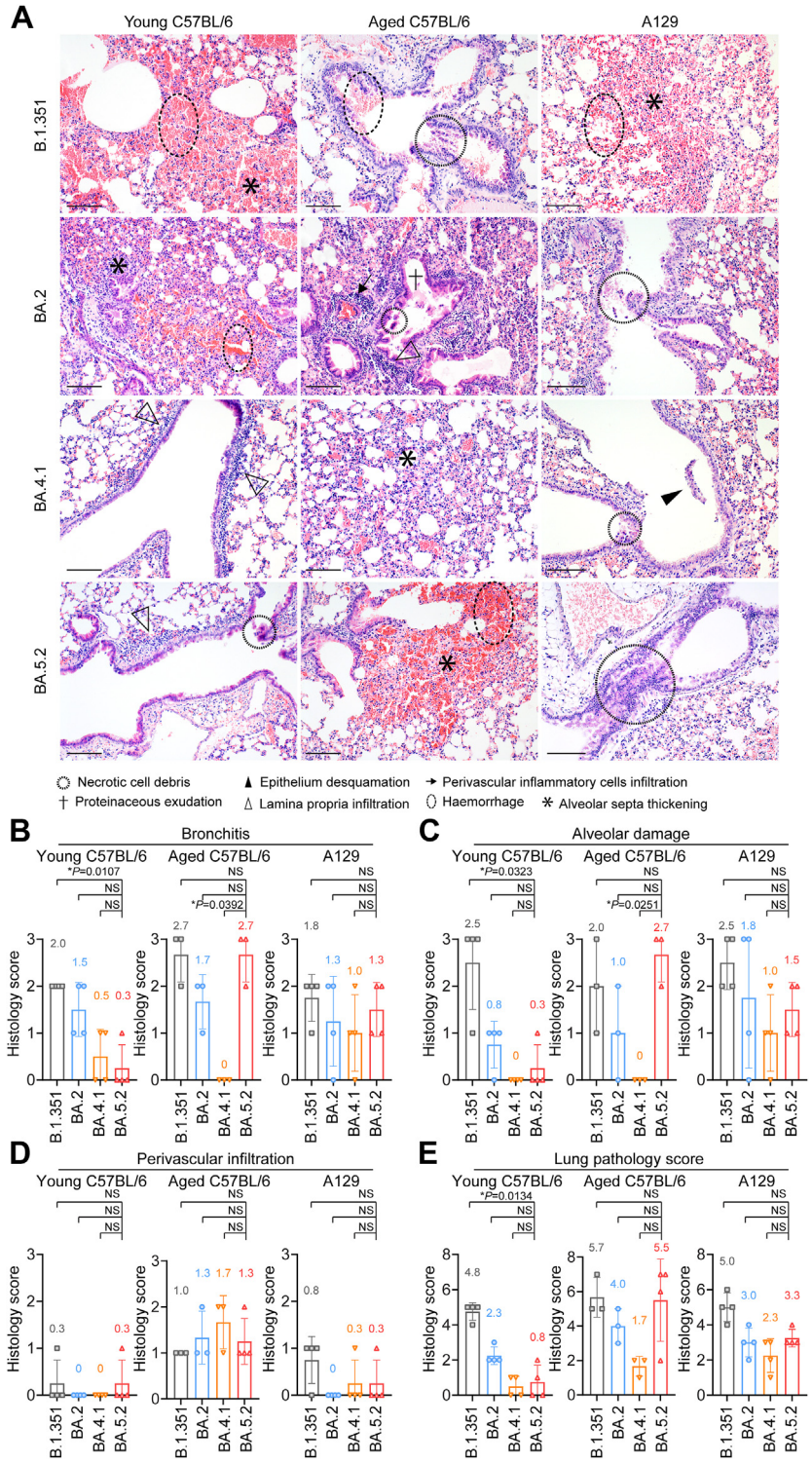

***Fig. 7*: Pathogenicity of Omicron BA.2, BA.4.1 and BA.5.2 in WT C57BL/6, aged C57BL/6, and A129 mice.** 6-to-8-week-old female C57BL/6, 10-to-11-month old female C57BL/6 and 6-to-8-week-old female A129 challenged with 1×10^5 PFU Omicron subvariants BA.2, BA.4.1, BA.5.2, or B.1.351 (Beta) and were euthanized at 2 dpi to collect lung tissues for pathological examination (n = 4 for young C57BL/6 and A129 mice, n = 3 for aged C57BL/6 mice). (**A**) Representative images of H&E staining of the nasal turbinate and lung. Dashed circles, necrotic cell debris; closed arrowheads, epithelium desquamation; arrows, perivascular inflammatory cell infiltration; cross, proteinaceous exudation; open

extensive alveolar destruction (Fig. 7A and C), and interstitial congestion with severe inflammatory infiltrations (Fig. 7A and D). In keeping with the viral antigen expression results in lungs of young C57BL/6 mice, the mean total lung pathology score of BA.5.2 (0.8) was lower than those of B.1.351 (4.8) and BA.2 (2.3). However, in aged C57BL/6 and A129 mice, the total lung pathology score of BA.5.2 was similar to those of B.1.351 and BA.2 (Fig. 7E). Together, our results demonstrate that the dominant Omicron sublineages are gaining replication fitness in both primary human nasal epithelial cells and nasal epithelium of infected animals. In contrast, the replication of all evaluated Omicron sublineages are attenuated in the lungs of K18-hACE2 and young C57BL/6 mice, leading to reduced lung pathology. Notably, the replication and pathogenicity of BA.5.2 remain comparable to BA.2 in the lungs of aged C57BL/6 and A129 mice, suggesting Omicron infection can still cause severe infection in the immunocompromised animals.

Discussion

Previous literature demonstrated that BA.1 had a replication advantage over Delta[29,30] and could outcompete Delta in co-infection experiments in human nasal epithelial cells.[31] However, the intrinsic replication fitness of Omicron sublineages in the nasal epithelium has not been thoroughly investigated. Here, we revealed that while all Omicron sublineages replicated substantially more robustly than that of WT in human nasal epithelial cells of the upper respiratory tract, the dominant Omicron sublineages BA.1, BA.2 and BA.5 are gaining further replication fitness in human nasal epithelial cells in the order of BA.1, BA.2, BA.4.1, and BA.5.2. In the nasal turbinates of K18-hACE2 mice, BA.5.2 replicated better than BA.2, which was in turn better than BA.1. In keeping with these results, BA.5.2 outcompeted BA.2 and BA.4.1 in in-vivo competition assays in the nasal turbinates of K18-hACE2 mice. Similarly, BA.5.2 consistently replicated to higher levels than BA.2 in the nasal turbinates of young C57BL/6, aged C57BL/6, and A129 mice. Concordantly, a recent study also demonstrated an increased replication capacity of BA.5 in the upper airway in ferrets.[32] Collectively, these findings indicate that the dominant Omicron sublineages, including BA.1, BA.2, and BA.5, have become increasingly efficient in their replication at the nasal epithelium of the upper respiratory tract. Increased viral replication fitness in the upper respiratory tract was associated with enhanced virus transmissibility in vivo.[33–36] Therefore, the intrinsically increased efficiency of Omicron replication in the nasal epithelium may contribute to their more efficient spread among the human populations observed clinically.[37–39]

In early 2022, we and others reported that BA.1 was attenuated in pathogenicity in vivo when compared to SARS-CoV-2 WT and previous VOCs.[4,8] This observation was later confirmed by additional in vivo studies[40,41] as well as recent clinical studies conducted in COVID-19 patients.[10–14] Subsequently, we reported that BA.2 replicated slightly less efficiently than BA.1 in the lungs of K18-hACE2 mice, resulting in slightly more attenuated lung pathology when compared to BA.1.[15] This finding was similarly confirmed in recent clinical studies. In a large cohort study in England that included over one million patients, BA.2 cases had lower risks of death and hospital admission than BA.1 after adjustment for confounders.[42] In another study from South Africa, the risk of severe disease among hospitalised individuals upon BA.2 infection was lower than that of BA.1 cases (adjusted odds ratio = 0.78; P = 0.029).[43] During the preparation of our manuscript, a study indicated BA.5 can infect lung cells more robustly than earlier Omicron subvariants both in vitro and in vivo.[32] Such discrepancies might be attributed to the amino acid substitutions in the viral genome as well as the differences in animal models used. The pathogenicity of BA.5 has been evaluated by additional groups but with inconsistent conclusions.[44,45]

In this study, we showed that the infectious titre and viral protein expression of BA.5.2 was 2.1- and 1.5-fold lower than that of BA.2 in the lungs of K18-hACE2 mice. Meanwhile, the total lung pathology score of BA.5.2 was 2.5-folds lower than that of BA.2, suggesting that BA.5.2 was slightly further attenuated when compared to BA.2. Since the receptor expression in the K18-hACE2 transgenic mice may not be optimally

arrowheads, lamina propria infiltration; dashed ellipse, haemorrhage; asterisk, alveolar septa thickening. Three sections were taken from each animal for immunochemistry analysis. Scale bar, 100 μm. (**B–E**) Semiquantitative analysis of the pathological changes in the lung. (**B**) Bronchiolitis (0 = normal structure; 1 = mild peribronchiolar infiltration; 2 = peribronchiolar infiltration plus epithelial cell death; 3 = score 2 plus intrabronchiolar wall infiltration and epithelium desquamation), (**C**) alveolar damage (0 = normal structure; 1 = alveolar wall thickening and congestion; 2 = focal alveolar space infiltration or exudation; 3 = diffused alveolar space infiltration or exudation or haemorrhage) and (**D**) perivascular infiltration (0 = normal structure; 1 = mild perivascular oedema or infiltration; 2 = vessel wall infiltration; 3 = severe endothelium infiltration) were scored accordingly. (**E**) Pathology scores of the of the lung were shown by adding up the histological scores of bronchiolitis, alveolar damage, and perivascular infiltration in the lung of each animal. Four mice from each experimental group were used for histology analysis and semiquantitative analysis. Statistical significance was determined with Kruskal–Wallis nonparametric test followed by Holm-Sidak's multiple comparisons test in (**B–E**). Data were obtained from three independent experiments. Each data point represents one biological repeat. Mean value for each experiment group were shown. *p < 0.05, **p < 0.01. NS, not statistically significant.

physiological, we additionally evaluated the replication and pathogenicity of BA.5.2 and BA.2 in wildtype C57BL/6 mice and A129 mice. Importantly, we found that the subgenomic E gene, infectious titre, and viral protein expression in lungs of BA.5.2-infected young C57BL/6 mice were 12.9- ($P = 0.0096$), 22- ($P = 0.0100$), and 11.3-folds ($P = 0.0266$) lower than that of BA.2-infected young C57BL/6 mice, respectively. In keeping with the virus replication results, the total lung pathological score of BA.5.2-infected young C57BL/6 mice was 2.9-folds lower when compared to that of BA.2-infected young C57BL/6 mice. Together, our results from K18-hACE2 and wildtype C57BL/6 mice indicate that the dominant Omicron sublineages, including BA.1, BA.2, and BA.5, continue to attenuate in replicating in the lungs, leading to attenuated pathogenicity. Nevertheless, in the lung tissue of immunodeficient aged C57BL/6 mice and the IFN alpha/beta receptor knockout A129 mice, BA.5.2 replicated to comparable level as BA.2 and could still result in severe lung diseases, suggesting that despite the attenuation of Omicron sublineages in the general populations with intact immunity, the ongoing transmission of Omicron sublineages remains a threat to the elderlies and immunocompromised patients. Therefore, vaccination is an important countermeasure to reduce hospitalization and to prevent the spread of SARS-CoV-2 in the immunocompromised population. However, since major differences regarding to virus tropism, transmissibility, clinical symptoms remain unneglectable between infected animal models and humans, continuous clinical surveillance to reflect the replication fitness and pathogenicity of Omicron sublineages in humans should be conducted in future studies.

We and others previously demonstrated that BA.1 and BA.2 spikes are characterized with reduced spike cleavage at the S_1/S_2 site, reduced efficiency in spike-mediated cell-cell fusion, reduced plaque formation, and decreased TMPRSS2 usage while increase in capacity in cell entry through the endocytic pathway.[7–9,15,21,24,46] In this study, we demonstrated that BA.5.2 spike had increased spike cleavage at the S_1/S_2 site and gained efficiency in spike-mediated cell-cell fusion leading to larger plaque size when compared with BA.1 and BA.2 spikes. Interestingly, the BA.4/5 spike pseudovirus was enhanced in utilizing the endosomal entry pathway when compared to the BA.2 spike pseudovirus, which cannot be explained by its increased spike cleavage and gained efficiency in spike-mediated cell-cell fusion. We further verified this observation by infection with authentic BA.1, BA.2 and BA.5 viruses and the data suggested BA.5 consistently showed reduced TMPRSS2-mediated virus entry while increased in dependency on the endocytic entry pathway when compared with wildtype SARS-CoV-2 and BA.1. Although discrepancies remained between our current study and findings from a recent study which suggested an enhanced TMPRSS2 usage for BA.5,[47] it should be aware that the predominant cell entry pathway utilized by SARS-CoV-2 is cell type-dependent. To this end, physiological-relevant cells or cell lines such as primary human airway cells should be used when investigating virus entry pathways.

While previous studies provided compelling evidence that suggested the spike gene is likely a major determinant of the observed virological and pathogenicity phenotypes of Omicron,[30,31] additional reports have also suggested major determinants of Omicron pathogenicity to reside outside of spike.[48,49] For example, nsp6 was shown to contribute to the attenuated pathogenicity of the Omicron BA.1, although detailed mechanism remained to be elucidated. The clinical isolate BA.5.2 that we used in the current study (GISAID: EPI_ISL_13777658) differs from BA.2 (GISAID: EPI_ISL_9845731) at multiple non-spike regions, including NSP3 (G489S), NSP4 (F438L), M (D3N) and ORF3 (F140L). Substitutions at these sites might also contribute to the discrepant pathogenicity of BA.5.2 in immunocompetent mice (K18-hACE2 and young C57BL/6) and immunodeficient mice (A129 and aged C57BL/6), as well as the differences between spike-only recombinant Omicron and authentic Omicron strains reported in previous studies.[15,16,24,32,44,45]

Overall, our study investigated the virological features, replication, and pathogenicity of the dominant Omicron sublineages for the past year (BA.1, BA.2, and BA.5). Our data suggested that the Omicron sublineages might be gaining replication fitness in the upper respiratory tract while that in the lung are continuously attenuated. These findings provide scientific foundations to the public health authorities for setting up control and management measures against the emerging Omicron sublineages.

Contributors

H.S., J.F.-W.C., B.H., Y.C., and C.Y. contributed equally to this work. H.S., B.H., and H.C. had roles in the study design, data collection, data analysis, data interpretation, literature search, and writing of the manuscript. H.S., J.F.-W.C., B.H., Y.C., C.Y., H.L., Y.L., J.S., J.-C.H., Y.H., X.H., T.T.-T.Y., T.Z., Y.W., J.Z., Y.X., Y.-F.H., L.-L.C., J.-P.C., J.Z., S.Y., A.J.Z., B.-Z.Z., J.-D.H., K.K.-W.T., K.-Y.Y., and H.C. performed experiments and/or analysed the data. H.C. oversaw the conception and supervised the study. H.S., J.F.-W.C., and H.C. provided funding support. All authors read and approved the final version of the manuscript. H.S., J.F.-W.C., B.H., Y.C., C.Y., and H.C. have accessed and verified the underlying data.

Data sharing statement

The data that support the findings of this study are available from the corresponding author upon reasonable request.

Declaration of interests

The authors declare no competing interests.

Acknowledgements

This work was partly supported by funding from National Natural Science Foundation of China Excellent Young Scientists Fund (Hong Kong and Macau) (32122001); the Health and Medical Research Fund

(COVID1903010-Project 14, 20190652), the Food and Health Bureau, The Government of the Hong Kong Special Administrative Region; the General Research Fund (17123920, 17118621), Collaborative Research Fund (C7103-22G, C7060-21G, C5033-19E), and Theme-Based Research Scheme (T11-709/21-N and T11-706/18-N), the Research Grants Council of the Hong Kong Special Administrative Region; Health@InnoHK, Innovation and Technology Commission, the Government of the Hong Kong Special Administrative Region; National Program on Key Research Project of China (grant no. 2020YFA0707500 and 2020YFA0707504); the Consultancy Service for Enhancing Laboratory Surveillance of Emerging Infectious Diseases and Research Capability on Antimicrobial Resistance for Department of Health of the Hong Kong Special Administrative Region Government, Sanming Project of Medicine in Shenzhen, China (No. SZSM201911014); the High Level-Hospital Program, Health Commission of Guangdong Province, China; General Programme, Guangdong Provincial National Science Foundation, China (2023A1515012325; 2023A1515011891); the University of Hong Kong Li Ka Shing Faculty of Medicine Enhanced New Staff Start-up Fund; the University of Hong Kong Outstanding Young Researcher Award; the University of Hong Kong Research Output Prize (Li Ka Shing Faculty of Medicine); the Major Science and Technology Program of Hainan Province (ZDKJ202003); the research project of Hainan Academician Innovation Platform (YSPTZX202004); the Hainan Talent Development Project (SRC200003); Emergency Collaborative Project (EKPG22-01) of Guangzhou Laboratory; and Emergency COVID-19 grant (2021YFC0866100) from Major Projects on Public Security under the National Key Research and Development Program of China; and donations from the Shaw Foundation Hong Kong, Richard Yu and Carol Yu, May Tam Mak Mei Yin, Michael Seak-Kan Tong, the Providence Foundation Limited (in memory of the late Lui Hac Minh), Lee Wan Keung Charity Foundation Limited, Hui Ming, Hui Hoy and Chow Sin Lan Charity Fund Limited, The Chen Wai Wai Vivien Foundation Limited, Hong Kong Sanatorium & Hospital, Chan Yin Chuen Memorial Charitable Foundation, Marina Man-Wai Lee, the Hong Kong Hainan Commercial Association South China Microbiology Research Fund, the Jessie & George Ho Charitable Foundation, Perfect Shape Medical Limited, Kai Chong Tong, Foo Oi Foundation Limited, Tse Kam Ming Laurence, Betty Hing-Chu Lee, Ping Cham So, and Lo Ying Shek Chi Wai Foundation. All donors and funding sources had no role in the study design, data collection, analysis, interpretation, or writing of the manuscript.

Materials and correspondence

Correspondence and material requests should be addressed to Dr. Hin Chu.

Appendix A. Supplementary data

Supplementary data related to this article can be found at https://doi.org/10.1016/j.ebiom.2023.104753.

References

1 Cao Y, Wang J, Jian F, et al. Omicron escapes the majority of existing SARS-CoV-2 neutralizing antibodies. *Nature*. 2022;602(7898):657–663.
2 Carreno JM, Alshammary H, Tcheou J, et al. Activity of convalescent and vaccine serum against SARS-CoV-2 Omicron. *Nature*. 2022;602(7898):682–688.
3 Cele S, Jackson L, Khoury DS, et al. Omicron extensively but incompletely escapes Pfizer BNT162b2 neutralization. *Nature*. 2022;602(7898):654–656.
4 Halfmann PJ, Iida S, Iwatsuki-Horimoto K, et al. SARS-CoV-2 Omicron virus causes attenuated disease in mice and hamsters. *Nature*. 2022;603(7902):687–692.
5 Iketani S, Liu L, Guo Y, et al. Antibody evasion properties of SARS-CoV-2 Omicron sublineages. *Nature*. 2022;604(7906):553–556.
6 Liu L, Iketani S, Guo Y, et al. Striking antibody evasion manifested by the Omicron variant of SARS-CoV-2. *Nature*. 2022;602(7898):676–681.
7 Meng B, Abdullahi A, Ferreira I, et al. Altered TMPRSS2 usage by SARS-CoV-2 Omicron impacts tropism and fusogenicity. *Nature*. 2022;603(7902):706–714.
8 Shuai H, Chan JF, Hu B, et al. Attenuated replication and pathogenicity of SARS-CoV-2 B.1.1.529 Omicron. *Nature*. 2022;603(7902):693–699.
9 Suzuki R, Yamasoba D, Kimura I, et al. Attenuated fusogenicity and pathogenicity of SARS-CoV-2 Omicron variant. *Nature*. 2022;603:700–705.
10 Ward IL, Bermingham C, Ayoubkhani D, et al. Risk of covid-19 related deaths for SARS-CoV-2 omicron (B.1.1.529) compared with delta (B.1.617.2): retrospective cohort study. *BMJ*. 2022;378:e070695.
11 Goncalves BP, Hall M, Jassat W, et al. An international observational study to assess the impact of the Omicron variant emergence on the clinical epidemiology of COVID-19 in hospitalised patients. *eLife*. 2022;11:e80556.
12 Wolter N, Jassat W, Walaza S, et al. Early assessment of the clinical severity of the SARS-CoV-2 omicron variant in South Africa: a data linkage study. *Lancet*. 2022;399(10323):437–446.
13 Nyberg T, Ferguson NM, Nash SG, et al. Comparative analysis of the risks of hospitalisation and death associated with SARS-CoV-2 omicron (B.1.1.529) and delta (B.1.617.2) variants in England: a cohort study. *Lancet*. 2022;399(10332):1303–1312.
14 Lewnard JA, Hong VX, Patel MM, Kahn R, Lipsitch M, Tartof SY. Clinical outcomes associated with SARS-CoV-2 Omicron (B.1.1.529) variant and BA.1/BA.1.1 or BA.2 subvariant infection in southern California. *Nat Med*. 2022;28(9):1933–1943.
15 Chan JF, Hu B, Chai Y, et al. Virological features and pathogenicity of SARS-CoV-2 Omicron BA.2. *Cell Rep Med*. 2022;3(9):100743.
16 Uraki R, Kiso M, Iida S, et al. Characterization and antiviral susceptibility of SARS-CoV-2 Omicron BA.2. *Nature*. 2022;607(7917):119–127.
17 Chu H, Hou Y, Yang D, et al. Coronaviruses exploit a host cysteine-aspartic protease for replication. *Nature*. 2022;609(7928):785–792.
18 Zhang BZ, Shuai H, Gong HR, et al. Bacillus Calmette-Guerin-induced trained immunity protects against SARS-CoV-2 challenge in K18-hACE2 mice. *JCI Insight*. 2022;7(11):e157393.
19 Chu H, Shuai H, Hou Y, et al. Targeting highly pathogenic coronavirus-induced apoptosis reduces viral pathogenesis and disease severity. *Sci Adv*. 2021;7(25):eabf8577.
20 Zheng J, Wong LR, Li K, et al. COVID-19 treatments and pathogenesis including anosmia in K18-hACE2 mice. *Nature*. 2021;589(7843):603–607.
21 Hu B, Chan JF, Liu H, et al. Spike mutations contributing to the altered entry preference of SARS-CoV-2 omicron BA.1 and BA.2. *Emerg Microbes Infect*. 2022;11(1):2275–2287.
22 Havranek KE, Jimenez AR, Acciani MD, et al. SARS-CoV-2 spike alterations enhance pseudoparticle titers and replication-competent VSV-SARS-CoV-2 virus. *Viruses*. 2020;12(12):1465.
23 O'Toole A, Hill V, Pybus OG, et al. Tracking the international spread of SARS-CoV-2 lineages B.1.1.7 and B.1.351/501Y-V2 with grinch. *Wellcome Open Res*. 2021;6:121.
24 Yamasoba D, Kimura I, Nasser H, et al. Virological characteristics of the SARS-CoV-2 Omicron BA.2 spike. *Cell*. 2022;185(12):2103–2115.e19.
25 Chu H, Hu B, Huang X, et al. Host and viral determinants for efficient SARS-CoV-2 infection of the human lung. *Nat Commun*. 2021;12(1):134.
26 Deprez M, Zaragosi LE, Truchi M, et al. A single-cell atlas of the human healthy airways. *Am J Respir Crit Care Med*. 2020;202(12):1636–1645.
27 Shuai H, Chan JF, Yuen TT, et al. Emerging SARS-CoV-2 variants expand species tropism to murines. *EBioMedicine*. 2021;73:103643.
28 Gu H, Chen Q, Yang G, et al. Adaptation of SARS-CoV-2 in BALB/c mice for testing vaccine efficacy. *Science*. 2020;369(6511):1603–1607.
29 Willett BJ, Grove J, MacLean OA, et al. SARS-CoV-2 Omicron is an immune escape variant with an altered cell entry pathway. *Nat Microbiol*. 2022;7(8):1161–1179.
30 Peacock TP, Brown JC, Zhou J, et al. The altered entry pathway and antigenic distance of the SARS-CoV-2 Omicron variant map to separate domains of spike protein, 2021.12.31.474653 *bioRxiv*. 2022. https://doi.org/10.1101/2021.12.31.474653.
31 Barut GT, Halwe NJ, Taddeo A, et al. The spike gene is a major determinant for the SARS-CoV-2 Omicron-BA.1 phenotype. *Nat Commun*. 2022;13(1):5929.
32 Hoffmann M, Wong LR, Arora P, et al. Omicron subvariant BA.5 efficiently infects lung cells. *Nat Commun*. 2023;14(1):3500.
33 Escalera A, Gonzalez-Reiche AS, Aslam S, et al. Mutations in SARS-CoV-2 variants of concern link to increased spike cleavage and virus transmission. *Cell Host Microbe*. 2022;30(3):373–387.e7.

34 Liu Y, Liu J, Plante KS, et al. The N501Y spike substitution enhances SARS-CoV-2 infection and transmission. *Nature*. 2022;602(7896):294–299.
35 Xia H, Yeung J, Kalveram B, et al. Cross-neutralization and viral fitness of SARS-CoV-2 Omicron sublineages. *Emerg Microbes Infect*. 2023;12(1):e2161422.
36 Saito A, Tamura T, Zahradnik J, et al. Virological characteristics of the SARS-CoV-2 Omicron BA.2.75 variant. *Cell Host Microbe*. 2022;30(11):1540–1555.e15.
37 Hansen CH, Friis NU, Bager P, et al. Risk of reinfection, vaccine protection, and severity of infection with the BA.5 omicron subvariant: a nation-wide population-based study in Denmark. *Lancet Infect Dis*. 2023;23(2):167–176.
38 Karim SSA, Karim QA. Omicron SARS-CoV-2 variant: a new chapter in the COVID-19 pandemic. *Lancet*. 2021;398(10317):2126–2128.
39 Tegally H, Moir M, Everatt J, et al. Emergence of SARS-CoV-2 omicron lineages BA.4 and BA.5 in South Africa. *Nat Med*. 2022;28(9):1785–1790.
40 McMahan K, Giffin V, Tostanoski LH, et al. Reduced pathogenicity of the SARS-CoV-2 omicron variant in hamsters. *Med*. 2022;3(4):262–268.e4.
41 van Doremalen N, Singh M, Saturday TA, et al. SARS-CoV-2 Omicron BA.1 and BA.2 are attenuated in rhesus macaques as compared to Delta. *bioRxiv*. 2022. https://doi.org/10.1101/2022.08.01.502390.
42 Webster HH, Nyberg T, Sinnathamby MA, et al. Hospitalisation and mortality risk of SARS-COV-2 variant omicron sub-lineage BA.2 compared to BA.1 in England. *Nat Commun*. 2022;13(1):6053.
43 Wolter N, Jassat W, Walaza S, et al. Clinical severity of SARS-CoV-2 Omicron BA.4 and BA.5 lineages compared to BA.1 and Delta in South Africa. *Nat Commun*. 2022;13(1):5860.
44 Kimura I, Yamasoba D, Tamura T, et al. Virological characteristics of the SARS-CoV-2 Omicron BA.2 subvariants, including BA.4 and BA.5. *Cell*. 2022;185(21):3992–4007.e16.
45 Uraki R, Halfmann PJ, Iida S, et al. Characterization of SARS-CoV-2 Omicron BA.4 and BA.5 isolates in rodents. *Nature*. 2022;612(7940):540–545.
46 Chan JF, Huang X, Hu B, et al. Altered host protease determinants for SARS-CoV-2 Omicron. *Sci Adv*. 2023;9(3):eadd3867.
47 Aggarwal A, Akerman A, Milogiannakis V, et al. SARS-CoV-2 Omicron BA.5: evolving tropism and evasion of potent humoral responses and resistance to clinical immunotherapeutics relative to viral variants of concern. *EBioMedicine*. 2022;84:104270.
48 Chen DY, Kenney D, Chin CV, et al. Role of spike in the pathogenic and antigenic behavior of SARS-CoV-2 BA.1 Omicron. *bioRxiv*. 2022. https://doi.org/10.1101/2022.10.13.512134.
49 Liu S, Selvaraj P, Sangare K, Luan B, Wang TT. Spike protein-independent attenuation of SARS-CoV-2 Omicron variant in laboratory mice. *Cell Rep*. 2022;40(11):111359.